Chapter 5

Bimetallic Pd-Ag Nanoclusters Decorated Micro-Cellulose Bio-Template for Catalytic Suzuki-Miyaura Coupling Reaction of N-Rich Heterocycles

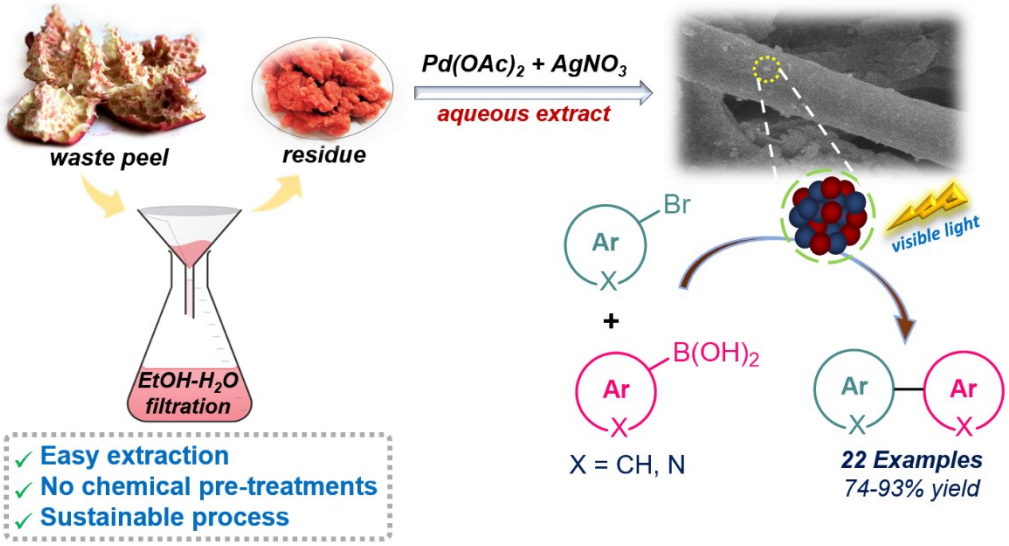

5.1 Introduction

Owing to the importance and widespread applicability of Suzuki-Miyaura cross coupling reactions, development of efficient catalytic strategies and extension of substrate scope for the reaction, cumulates immense significance and interest [1,2]. Subsequently, development of ligand-free heterogeneous catalysts using bio-based renewable supports become important [3]. Among the various bio-based supports used, cellulose is unique in terms of its high abundance, chemical inertness, high specific surface area, dimensional stability, available surface functional bonds, and biodegradability [4,5]. In recent times, successful extraction of cellulose in micro- and nano-crystalline forms [6] have rendered its use as a support template for various metallic nanoparticles (NPs) such as Pd [7,8], Au [9], Ag [10], and bi-metallic Fe-Cu [11], Ag-Cu [12], Ag-Au [13], NPs. Thus, cellulose in the form of nanostructures has been celebrated as one of the most prominent green templates for the synthesis of metal NPs.

The extraction and isolation of nanocellulose from biomass involve some vigorous pre-treatment processes [14], directing the elimination of non-cellulosic components, such as polymers of free sugar, fatty acids, flavonoids, terpenoids, hemicellulose and lignin [15], carried out in a number of chemical, mechanical, and combined methods [14,16]. A typical approach generally involves, alkali treatment with a strong base (NaOH), followed by bleaching with H_2O_2, $NaClO_2$, etc., and finally acid hydrolysis using strong mineral acids [16]. Although the methods are effective as it is claimed but there are some serious concerns to mark. Conventional pre-treatments are lengthy involving more than 40% of the total processing cost and energy consumption [17]. Also, the use of harsh chemicals for cellulose extraction leads to the generation of toxic and hazardous wastes, material contamination, and overall environmental stress [14]. Recently, a variety of advanced methods such as ionic liquid treatments [18], use of deep eutectic solvents [19], microwave [20], and ultrasonic treatments [21], have also been explored. In this regard, development of a simple extraction method to isolate cellulose fibers from waste fruit peels goes in line with green chemistry and sustainability.

In the modern era of nanotechnology, bimetallic NPs have conquered massive attention as combination of two different metals permit tuning of physical and

chemical properties of the bimetallic system leading to enhancement of the features of nanostructures in comparison with its monometallic counterparts [22].

Regarding catalytic applications, majority of the Pd-based nanostructures have been fully assessed for C–C coupling of conventional arylated substrates [23]. However, the methods failed to maintain its efficacy when more challenging nitrogen-based heterocycles are employed as one or both of the coupling partners [24]. Only a few direct cross-coupling reactions involving hetero-aryl moieties have been disclosed so far [24-33]. Recently, integration of Ag in various Pd-based reactions has witnessed significant improvement in organic transformations [34]. Comparing the electronic properties of both the precious-metals (Ag, Pd) unveils a favourable electron transfer possible from Ag to Pd as evident from their fermi energy levels [35,36]. This charge transfer from Ag atoms to Pd atoms is due to the net difference in electronegativity of both the metals (electronegativity values of Ag: 1.93 and Pd: 2.20). Bi-metallization of Ag nanoparticles with Pd nanoparticles would significantly help in modification of morphology and surface electronic structure of Pd nanoparticles, improving its catalytic performance and resistance. Thus, encouraging to explore this unique synergy for C–C coupling of challenging substrate combinations.

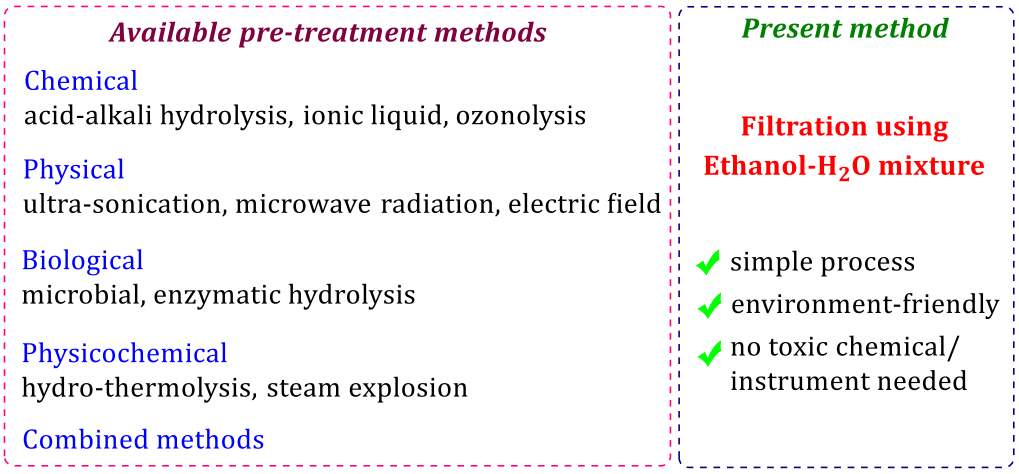

Figure 5.1 Previous and present approaches for extraction of cellulose fibers from plant biomass

Pomegranate peels which constitute about 50% of the total fruit, is a major source of waste cellulosic biomass [37]. This chapter presents the development of a simple filtration method using water-ethanol mixture to generate micro-cellulose bio-template from waste pomegranate peel residue (Figure **5.1**) and utilize it for the

synthesis and immobilization of Pd-Ag nanoparticles. The newly developed heterogeneous catalyst is efficiently employed in Suzuki-Miyaura cross-coupling reaction of nitrogen-rich heteroaromatics under the framework of green chemistry principles.

5.2 Results and Discussion

5.2.1 Green Synthesis of Cellulose Supported Pd-Ag Bi-Metallic Nanoclusters

In this chapter, isolation of cellulosic material from waste pomegranate peels have been achieved in a simple and eco-friendly extraction technique. The micro-fibrous network of cellulose functions as a true bio-template for immobilization of Pd-Ag bimetallic nanoclusters (Pd-Ag@PMFC). Presence of high-density polyphenolic compounds identified as gallic acid, ellagic acid, chlorogenic acid, caffeic acid, punicalin, among others present in peel extract act as bio-reducing agents and thus no external chemical reducing agent was required [38]. The hydroxyl groups on the surface of the cellulose matrix serves as nucleation point for Pd-Ag NPs on the solid support, thus leading to their incorporation and stabilization on the cellulose surface [39]. It is interesting to note that the pomegranate peel biomass residue used in the process was only subjected to washing by filtration using a water-ethanol solvent system and not exposed to any harsh chemical pre-treatments. It is expected that the ethanol-water mixture used in the process helps in solubilizing most of the lignin and other impurities from the biomass [40]. Thus, the peel residue finally obtained is rich in the cellulosic component. Since ethanol as a solvent has low toxicity and is relatively low-cost, thus presenting a simple, easy and sustainable extraction of cellulose from waste peel biomass.

5.2.2 Characterization of Pd-Ag@PMFC

The formation and validation of bio-mass derived Pd-Ag@PMFC was confirmed by analytical techniques such as transmission electron microscopy (TEM), scanning electron microscopy (SEM), powder X-ray diffraction (PXRD), energy dispersive X-Ray (EDX), X-ray photoelectron spectroscopy (XPS), Fourier Transform Infrared (FT-IR) spectroscopy, inductively coupled plasma-optical emission spectrometry (ICP-OES), thermogravimetric analysis (TGA), ultraviolet-visible (UV-Vis) spectrophotometry and Brunauer-Emmett-Teller (BET) surface area analyses.

The surface structure and the morphologies of the prepared nanomaterial were observed by SEM. The SEM images of the material clearly show the presence of thread-like fibrous structure of width around 8 µm onto which the NPs are supported (Figure **5.2a-b**). This reveals that pomegranate-peel derived micro-fibers of cellulose (PMFC) have been extracted using a simple ethanol-water mixture without any chemical treatments or sophisticated instruments.

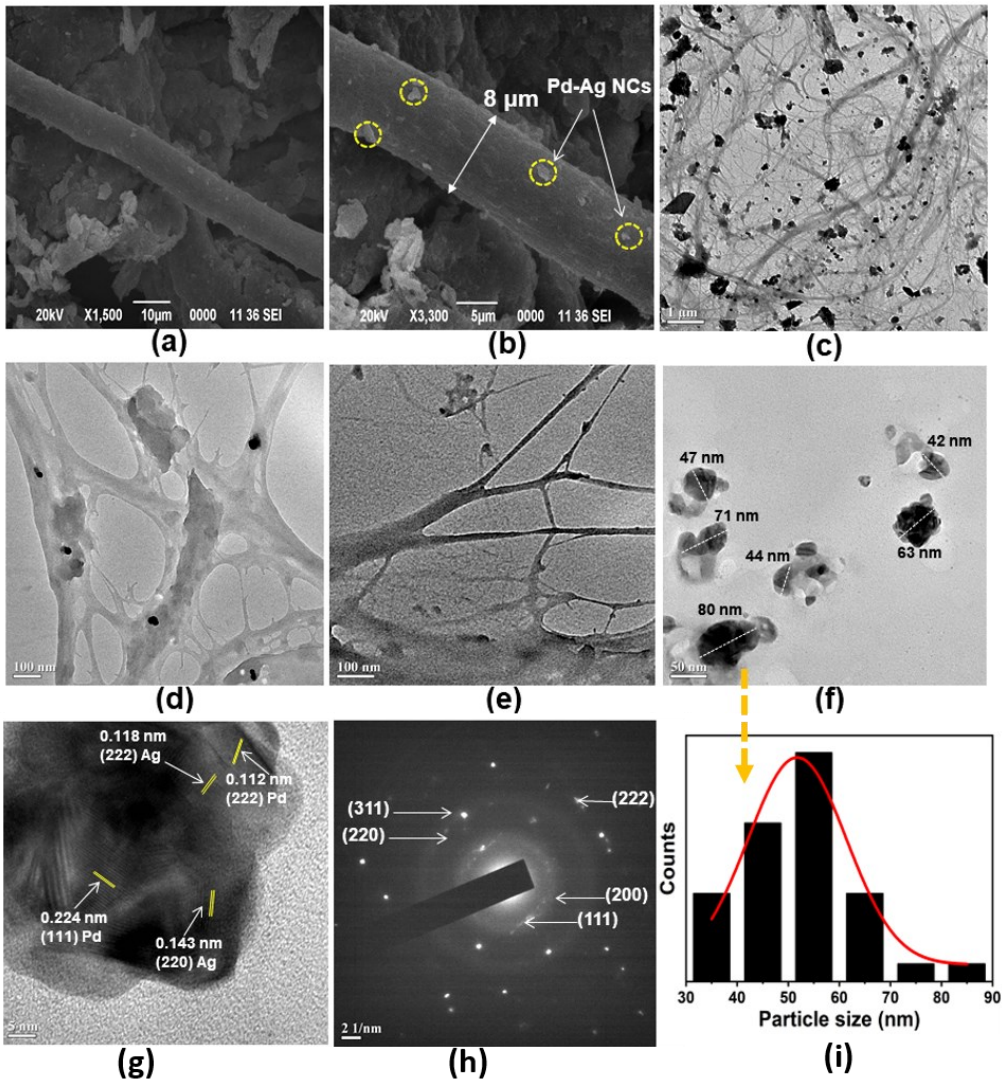

Figure 5.2 (a, b) SEM images, (c-f) TEM images, (g) HRTEM image, (h) SAED pattern, and (i) particle size distribution histogram, of Pd-Ag@PMFC

The low-resolution TEM confirmed the formation of thread-like fibrous network of the cellulosic-biomass which acts as a reinforcement material for the bio-genic Pd and Ag NPs embedded on it (Figure **5.2c-e**). From Figure **5.2f**, it can be observed that the Pd and Ag are present as spherical bi-metal nanoclusters (NCs) of homogeneous

size. The average particle size of spherical bi-metallic NCs was found to be 52 nm (Figure **5.2i**). The cellulose fibers contribute significantly to the good dispersion of the NCs within the support by preventing the formation of massive aggregates.

High-resolution TEM (HRTEM) images (Figure **5.2g**) of the NCs shows lattice fringes, which confirmed the presence of both the metallic counterparts in a single spherical cluster from the interplanar distance of 0.224 nm and 0.112 nm, which correspond to (111) and (222) crystal planes of Pd and similarly 0.118 nm and 0.143 nm interplanar spacings corresponding to (222) and (220) crystal planes in Ag. These results indicate the formation of bimetallic nanoclusters supported on micro-fibers of cellulose (Pd-Ag@PMFC). The corresponding selected-area electron diffraction (SAED) pattern (Figure **5.2h**) shows the presence of five well-resolved rings that can be attributed to (111), (200), (220), (311) and (222) lattice planes of the fcc bimetallic Pd-Ag NCs.

The elemental composition profile of Pd-Ag@PMFC was assessed by EDX analysis. According to the study (Figure **5.3**), the sample is found to hold a high atomic content of C (69.80%) and O (25.47%). The Pd:Ag atomic ratio in the sample appears to be 1.69:1.84, consistent with the ratio of respective metal precursors used (1:1). The high value of carbon is accredited to the organic biomass backbone of support and O atom from surface hydroxyl groups present on the PMFC support. Traces of some other elements such as Cl, Ca are also detected.

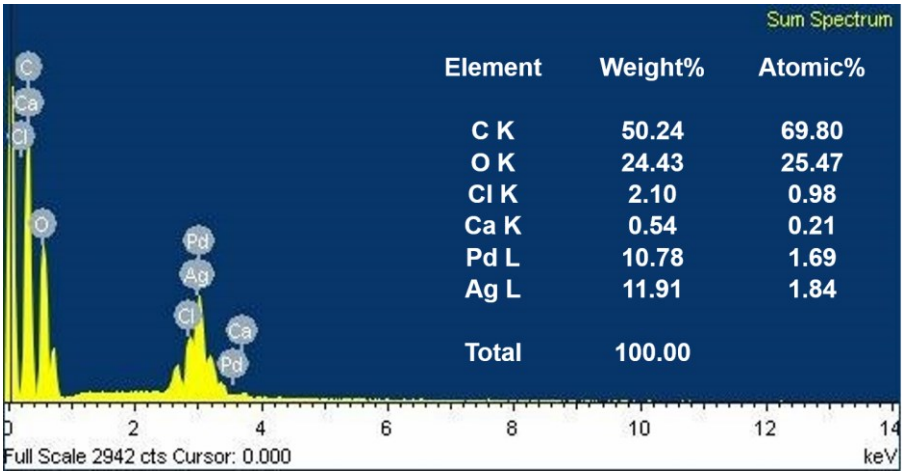

Figure 5.3 EDX spectrum of Pd-Ag@PMFC

In addition, Figure **5.4a** shows the electron image of Pd-Ag@PMFC and corresponding EDX elemental mapping of Pd (green), Ag (blue) and C (red) elements

(Figure **5.4b-d**). It reveals that the supported bimetallic Pd and Ag are all uniformly distributed and overlapped with each other in the support. These results are in good agreement with HRTEM images confirming the bi-metallization of Pd-Ag NCs homogeneously dispersed on the support. Moreover, ICP-OES analysis revealed that 1 g of solid Pd-Ag@PMFC contains 14.5 mg of Pd and 15.7 mg of Ag, respectively.

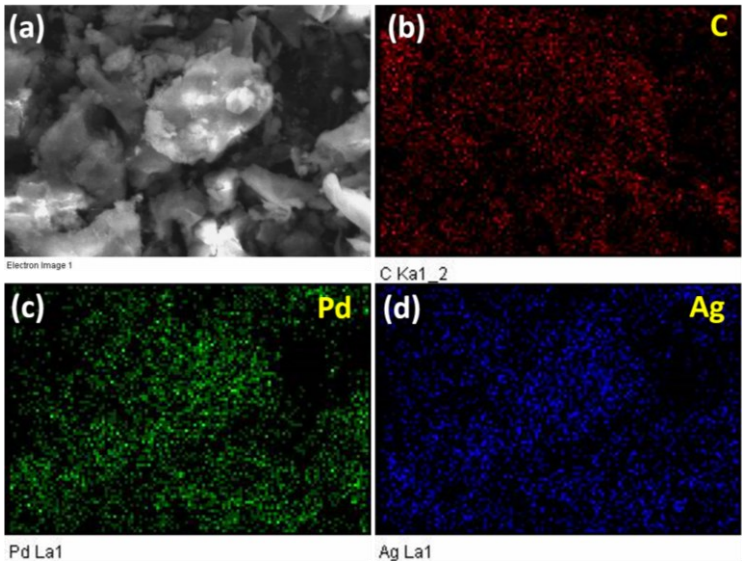

Figure 5.4 (a) Electron image, and corresponding (b-d) EDX elemental mapping images, of Pd-Ag@PMFC

The crystal phase information profile was acquired by PXRD studies shown in Figure **5.5a**. The XRD pattern of PMFC shows an intense peak at 2θ of 21.98° which is due to the presence of carbon backbone with C (002) in the crystalline cellulose support. After the incorporation of Pd-Ag, the broad diffraction peak at 21.98° disappeared and well-defined new diffraction peaks are detected. A strong diffraction peak appears at 2θ value 38.87°, which is located in-between the values of (111) crystal planes for pure Ag (38.1°) and pure Pd (40.1°). Similarly, diffraction peaks appearing at 2θ values: 45.16°, 46.45°, 65.53°, 67.33°, 76.82°, 79.02° can be assigned to the (200)Ag, (200)Pd, (220)Ag, (220)Pd, (311)Ag and (311)Pd crystallographic planes of fcc crystalline Ag-Pd bi-metallic system, respectively. The peak positions of Pd and Ag in Pd-Ag@PMFC are in good agreement with the standard JCPDS card no.- 87-0641 of Pd and 87-0719 of Ag. Apart from the Bragg's peaks characteristic for fcc Pd and Ag, a few additional peaks (marked with stars) at 28.08°, 32.47°, 55.05°, 57.64° were also detected. These are probably due to the crystallization of cubic mineral phase of some silver (AgCl) consistent with the (111), (200), (311), (222) planes,

respectively (JCPDS card no.- 31-1238), co-existing with the Ag NPs. Similar results have been often found in literature for Ag NPs prepared by various biogenic methods using $AgNO_3$ as the metal precursor, such as Geranium leaf extract [41], edible mushroom extract [42], *Coleus aromaticus* leaf extract [43].

FT-IR spectroscopic measurements were carried out to illustrate the possible functional groups contributing as reductants and stabilizers in the bio-reduction of metal precursors (Figure **5.5b**). FT-IR spectra of PMFC showed several distinct vibration bands including a broad and intense peak centred at 3437 cm^{-1}, indicate the presence of hydroxyl groups on the surface of cellulose biomass. Since the major component in a cellulosic material mainly constitutes O–H groups and many C–H (organic) fragments in its structure, the peak at 2924 cm^{-1} belongs to sp^3 hybridized –CH, $-CH_2$, and $-CH_3$ bond stretching vibrations. Peak at 1735 cm^{-1} is due to the presence of C=O group in the components of biomass and two peaks at 1020 cm^{-1} and 620 cm^{-1} is assigned for C–O group [44]. For comparison, the bi-metal loaded Pd-Ag@PMFC was also characterized by FT-IR spectroscopy. A slight shift in frequency values of some of the IR bands indicate the complexation of bi-metal Pd-Ag NCs on the support.

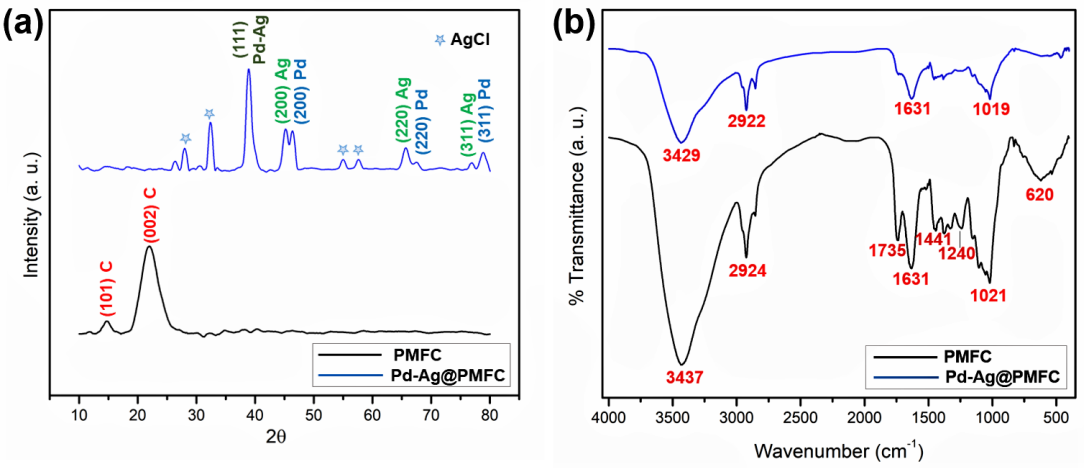

Figure 5.5 (a) Powder XRD patterns, (b) FT-IR spectra, of PMFC and Pd-Ag@PMFC

The thermal behaviour and stability of PMFC before and after bi-metal loading was determined by TGA (Figure **5.6**). The obtained weight loss versus temperature curve showed a mass loss of 6.80% for PMFC and 4.99% for Pd-Ag@PMFC at temperature around 100 °C, which corresponds to the adsorbed moisture in the samples. The

materials are found to sustain thermal variations and maintained their stability up to 225-230 °C after which a steep loss of 41-50% weight occurred, reflecting the decomposition of major organic components of the bio-derived materials.

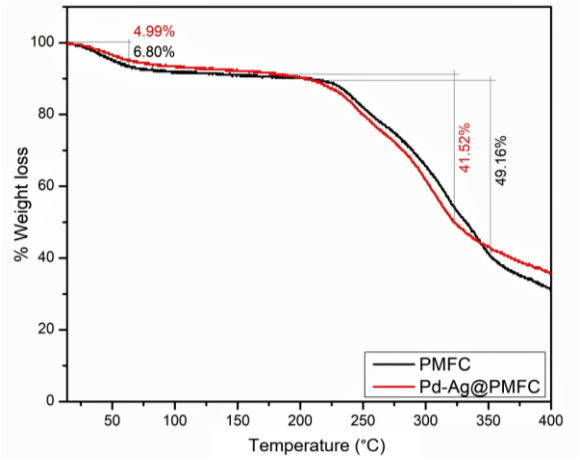

Figure 5.6 TGA curves of PMFC and Pd-Ag@PMFC

The specific surface area and porosity of the samples were investigated using BET N_2 adsorption-desorption measurement. The isotherm for PMFC (Figure **5.7a**) and Pd-Ag@PMFC (Figure **5.7b**) resembled the typical type IV of adsorption isotherms, which are characteristic of mesoporous structures involving strong adsorbate-adsorbent interactions. The desorption isotherm appeared at the top of the adsorption isotherm, accompanied by producing H3 hysteresis loops [45].

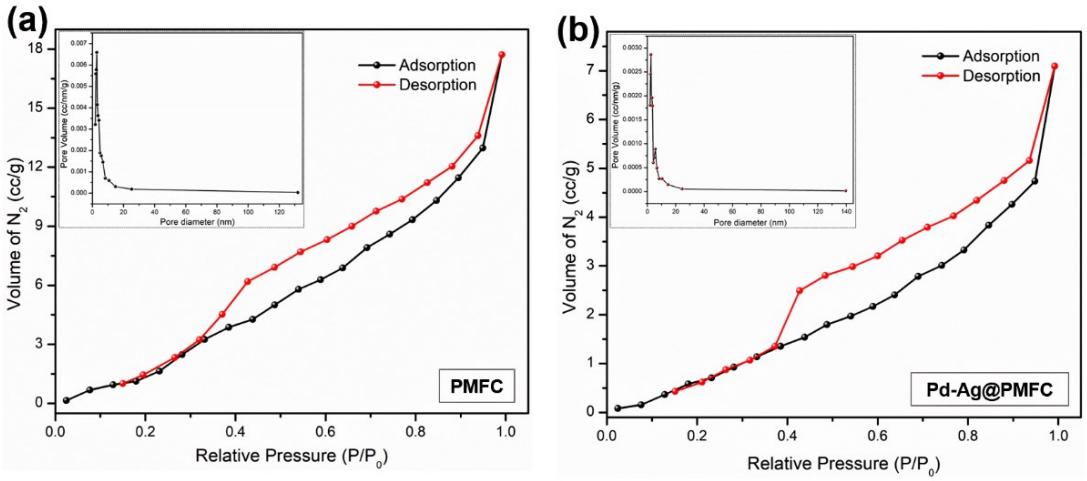

Figure 5.7 N_2 adsorption/desorption isotherms of (a) PMFC, (b) Pd-Ag@PMFC, and inset in (a, b) shows the BJH pore size distribution curves

Figure **5.7a** shows the BET investigations for PMFC with a calculated surface area of 50.457 m^2/g which significantly reduced to 11.760 m^2/g after bi-metal loading in Pd-

Ag@PMFC (Figure **5.7b**). This reveals the high adsorption efficiency of the natural support material, resulting in a strong interaction between Pd-Ag NCs and PMFC mesoporous framework, thereby decreasing its specific surface area. The results were further confirmed by the Barrett-Joyner-Halenda (BJH) pore size distribution (inset Figure **5.7a-b**). The distribution curve revealed the reduction in pore diameter from 3.863 nm to 2.437 nm and pore volume from 0.031 cm^3/g to 0.010 cm^3/g on bi-metal loading on the support. Thus, confirming that the Pd-Ag NCs are strongly embedded on the mesoporous surface of PMFC.

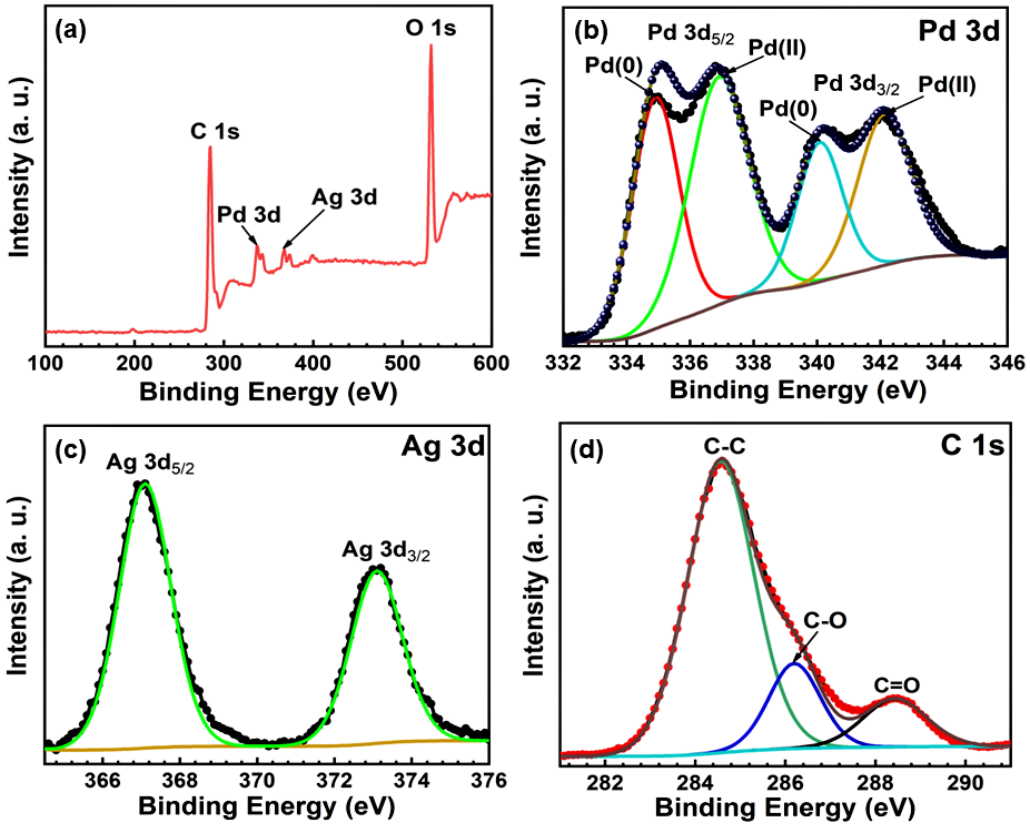

Figure 5.8 (a) Survey scans XPS spectrum of Pd-Ag@PMFC, and corresponding high-resolution deconvoluted XPS spectra of (b) Pd 3d, (c) Ag 3d, and (d) C 1s

The electronic information and the existing state of Pd and Ag in Pd-Ag@PMFC were studied using XPS analysis. Figure **5.8a** shows the survey scans XPS spectrum in existence with four sharp binding energy peaks which are attributed to C, Pd, Ag and O, respectively present in Pd-Ag@PMFC. The high-resolution Pd 3d spectrum is fitted with four binding energy peaks and the two spin-orbit doublets are ascribed to the Pd $3d_{5/2}$ and Pd $3d_{3/2}$ (Figure **5.8b**). The binding energy peaks at 334.9 eV and 340.1 eV correspond to the Pd(0) NPs and peaks located at 336.9 eV and 342.1 eV belong

to the Pd(II), respectively [46]. The high-resolution Ag 3d spectrum obtained with two sharp binding energy peaks attributed to the spin-orbit splitting of Ag $3d_{5/2}$ and Ag $3d_{3/2}$ (Figure **5.8c**) [47]. The binding energy peaks located at 367.1 and 373.1 eV of deconvoluted Ag 3d spectrum support the formation of Ag(0) NPs. The high-resolution C 1s spectrum fitted with three peaks confirmed the presence of PMFC support (Figure **5.8d**). The peaks at binding energies of 284.6, 286.2 and 288.4 eV correspond to C–C, C–O, and C=O functional bonds in PMFC, respectively.

5.2.3 Optimization of Reaction Conditions

To determine the efficiency of the as-synthesized Pd-Ag@PMFC towards the Suzuki-Miyaura cross-coupling reaction (SMCR), the reaction between 3-bromopyridine (**1a**) and phenylboronic acid (**2a**) was assessed as model substrates as represented in Table **5.1.**

Table 5.1 Screening of reaction conditions for SMCR[a]

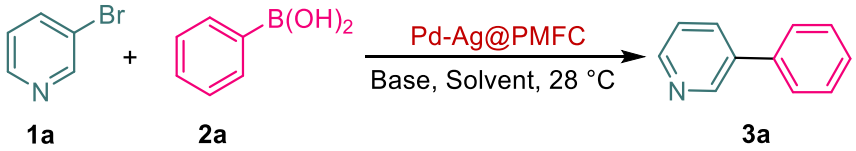

1a **2a** **3a**

Entry	Catalyst (wt%)	Solvent	Base	Time (h)	Yield (%)[b] of **3a**
1	15	EtOH	K_2CO_3	12	76
2	15	*i*-PrOH	K_2CO_3	12	72
3	15	CH_3CN	K_2CO_3	12	70
4	15	H_2O	K_2CO_3	10	83
5	15	H_2O-EtOH (1:1)	K_2CO_3	6	93
6	15	H_2O-EtOH (1:1)	Na_2CO_3	7	87
7	15	H_2O-EtOH (1:1)	Cs_2CO_3	6	92
8	15	H_2O-EtOH (1:1)	$NaHCO_3$	7	73
9	15	H_2O-EtOH (1:1)	NaOH	7	60
10	15	H_2O-EtOH (1:1)	KOH	7	63
11	15	H_2O-EtOH (1:1)	Et_3N	12	35
12	15	H_2O-EtOH (1:1)	-	24	nr
13	10	H_2O-EtOH (1:1)	K_2CO_3	6	93

14	8	H_2O-EtOH (1:1)	K_2CO_3	12	81
15	5	H_2O-EtOH (1:1)	K_2CO_3	12	65
16	-	H_2O-EtOH (1:1)	K_2CO_3	24	nr

[a]Reaction conditions: **1a** (0.5 mmol), **2a** (0.6 mmol), Pd-Ag@PMFC, base (1.2 mmol), solvent (4 mL), rt (28 °C); [b]isolated yield; nr (no reaction).

Initially, the catalytic performance was assessed under different conditions of base and solvent at room temperature (28 °C) with 15 wt% of the bio-derived catalyst. In order to optimize a proper solvent system, lower alcoholic solvents such as EtOH and *i*-PrOH and aprotic solvent CH_3CN were screened using K_2CO_3 as base which resulted in 70-76% of product yields in 12 h (Table **5.1**, entries **1-3**). Then, a reaction was carried out in pure aqueous media, which resulted in 83% of cross-coupled product in 10 h (Table **5.1,** entry **4**). However, the best result was obtained with a solvent media of EtOH and H_2O taken in 1:1 (v/v) ratio, both of which is considered as promising sustainable solvents for green chemistry. The system showed an enhancement in the product formation to 93% with a rapid drop in reaction time to 6 h (Table **5.1**, entry **5**). The possible reason behind such an acceleration in rate can be explained from the microscopic phase separation existing between two phases-aqueous-organic phase (where heteroaryl bromide is present) and aqueous-basic phase holding arylboronic acid and K_2CO_3. Thus, the coupling reaction efficiently occurs at the organic-water interface, and the interface area attained is maximum when EtOH-H_2O ratio is close to one, leading to 'on-water' acceleration effect [48]. Also, in presence of water, the nitrogen atoms present in the heterocyclic substrate prefer to engage in H-bonding with water rather than coordinating to the metal catalyst, resulting in much higher catalytic conversions. Next, in order to optimize a suitable base for the current reaction, a variety of common bases for SMCR were examined (Table **5.1**, entries **5-11**). Among them K_2CO_3 and Cs_2CO_3 showed highest activity with the reaction yield of 92-93% (Table **5.1**, entries **5**, **7**). However, considering the hygroscopic nature and the high cost of Cs_2CO_3, while K_2CO_3 is cheap, abundant, environmentally friendly, and non-toxic, making it an obvious choice for the study. However, the reaction did not proceed in the absence of a base (Table **5.1**, entry **12**). The amount of catalyst loading is another key parameter of a reaction. It was observed that lowering the amount to 10 wt% of the Pd-Ag@PMFC could

maintain the efficacy of the cross-coupled product (Table **5.1**, entry **13**). Further lowering in the amount from 10 wt% to 8 wt% and 5 wt% of catalyst caused a gradual decrease in the reaction yield and the reaction did not reach to completion even after prolonged reaction time. (Table **5.1**, entries **14-15**). The presence of a catalyst is a requirement for the transformation (Table **5.1**, entry **16**). Finally, investigating the influence of temperature on the current reaction showed an interesting result. The coupling reaction of *N*-heteroaryl substrate proceed to completion at room temperature under the present catalyst system.

5.2.4 Substrate Scope Study

With the optimized condition in hand, the potential of the catalyst system was determined for electronically diverse *N*-heteroaromatic substrates. Table **5.2** summarizes the survey of SMCR of *N*-heteroaryl bromides with arylboronic acids.

Table 5.2 SMCR of *N*-heteroaryl bromides and arylboronic acids[a]

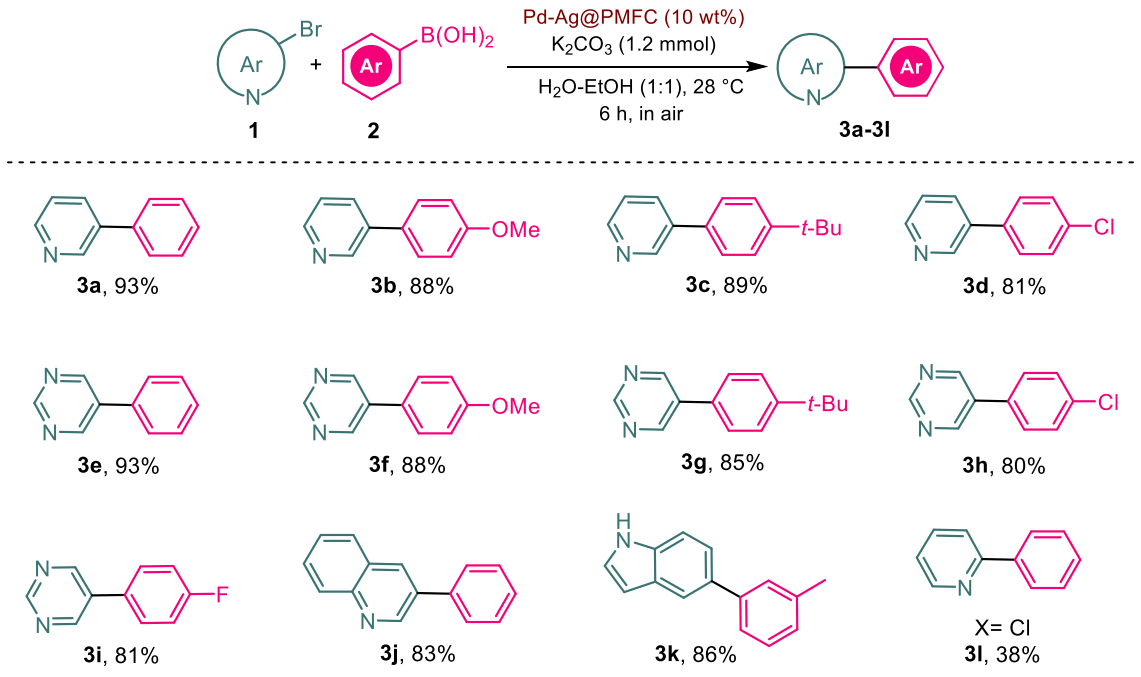

[a]Reaction conditions: **1** (0.5 mmol), **2** (0.6 mmol), Pd-Ag@PMFC (10 wt%, 0.001 mmol of Pd), K_2CO_3 (1.2 mmol), H_2O-EtOH 1:1 (4 mL), rt (28 °C), time (6 h); the yields reported are the isolated yields.

Interesting results were achieved with a variety of heteroaryl halide partners bearing pyridine, pyrimidine, quinoline and indole ring systems. 3-bromopyridine reacted

well with substituted (4-OMe, 4-*t*-Bu, 4-Cl) and unsubstituted arylboronic acid derivatives and produced the coupling product in decent yields (81-93%) (Table **5.2**, **3a-3d**). 5-bromopyrimidine also reacted with electron rich (-OMe, -*t*-Bu) and electron deficient (-Cl, -F) arylboronic acids forming desired products in good yields (80-93%) (Table **5.2**, **3e-3i**). In the similar trend, 3-bromoquinoline coupled with phenylboronic acid producing 83% yield of the reaction (Table **5.2**, **3j**). It is believed that the coupling reactions of aryl bromides with electron-poor substituents facilitate the oxidative addition step more effectively, resulting in higher substrate conversions. This is in agreement with the π-electron deficient heterocyclic core of pyridine, pyrimidine and quinoline substrates, giving admirable results for the coupling reaction at ambient temperature of 28 °C. An example of 5-bromoindole with phenylboronic acid is also shown. To our delight, desired coupling product was obtained in 86% yield (Table **5.2**, **3k**). When tested with a chloride coupling partner, 2-chloropyridine could produce only 38% of the coupled-product (Table **5.2**, **3l**).

Coupling reactions with heteroarylboronic acids are often considered to have more complications than heteroaryl halide partners. This is particularly concerning their stability that heteroarylboronic acids are prone to rapid decomposition *via* protodeboronation under basic media [49]. Making them potential challenging substrates, only a few literatures could represent their practical applicability. In the desire to test its reactivity under the present protocol, an attempt was made to study the coupling between simple aryl halides and *N*-heteroarylboronic acids (Table **5.3**).

At first, 3-pyridineboronic acid was reacted with 4-bromoanisole which produced the coupling product in 74% yield with a relatively long reaction time (Table **5.3**, **6a**). This reduced reactivity may be rationalized from the electron deficiency of the pyridine ring, which deliberately slows down the rate of transmetalation step. This problem could be resolved by introducing an electron-donating substituent (-OMe) in pyridineboronic acid moiety which elevated the reactivity of the same than its unsubstituted counterpart. Several substrate combinations containing both electron-rich (-OMe) and electron-poor (-NO_2, -COMe) aryl bromides were showed which coupled with 2-methoxy-5-pyridineboronic acid in quantitative yields (81-89%) (Table **5.3**, **6b-6d**). 5-indoleboronic acid was also assessed in the current system,

when reacted with 2-bromotoluene, the desired coupled product was obtained in 81% yield (Table **5.3**, **6e**).

Table 5.3 SMCR of aryl bromides and *N*-heteroarylboronic acids[a]

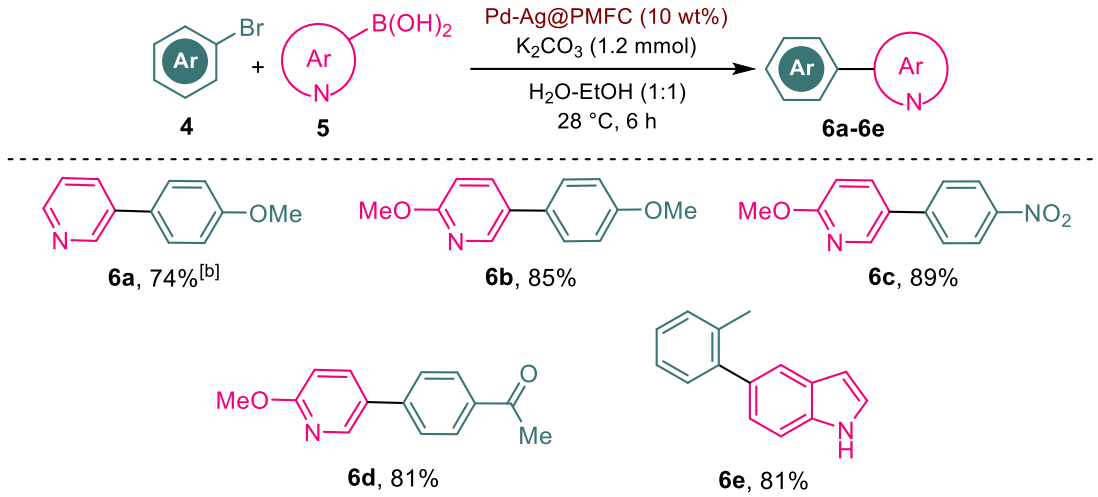

[a]Reaction conditions: **4** (0.5 mmol), **5** (0.6 mmol), Pd-Ag@PMFC (10 wt%, 0.001 mmol of Pd), K_2CO_3 (1.2 mmol), H_2O-EtOH 1:1 (4 mL), rt (28 °C), time (6 h); [b]time (12 h); the yields reported are the isolated yields.

It is seen that despite potential challenges of the heteroaromatic boronic acids, fairly acceptable reaction yields could be attained. To highlight the catalytic applicability of Pd-Ag@PMFC further, it was employed as a catalyst in SMCR between *N*-heteroaryl bromides and *N*-heteroarylboronic acids (Table **5.4**). Coupling reaction in which both the coupling partners contain nitrogen donors appear most challenging. The reaction of 3-bromopyridine with 3-pyridineboronic acid failed to exhibit any quantitative conversion to the desired product (Table **5.4**, **7a**). The reason being the electron-deficiency of heteroarylboronic acid counterpart. However, SMCR with electron-rich methoxy-substituted pyridineboronic acid gives 88% of isolated yield with 3-bromopyridine (Table **5.4**, **7b**). Inspired by the result, a variety of *N*-heteroaryl bromides namely 5-bromopyrimidine, 3-bromoquinoline and 5-bromoindole were reacted successfully with 2-methoxy-5-pyridineboronic acid affording significant yields (78-83%) of C–C coupled products (Table **5.4**, **7c-7e**). The results unfold a minor substituent effect of the *N*-heteroaryl bromide on the reaction rate. Our catalytic method was found to be inert to the free *N*–H group of indoles which shows its superiority to many other earlier systems where the *N*–H group is found to

deactivate the metal (Pd) catalyst [29]. In most of the examples, the homocoupling product was observed in less than 10% yield of the cross-coupled product. Hence, it can be concluded that following the principles of green chemistry, the present reaction protocol appeared highly active, selective, and stable towards SMCR in *N*-heteroaromatic system. Despite the presence of nitrogen heteroatoms, that might be expected to significantly affect the course of Pd catalyzed reaction of heteroaryl halides with heteroarylboronic acid, a wide variety of hetero-biaryl substrates have been successfully prepared and characterized having potential as key synthetic precursors for the construction of various bio-active compounds.

Table 5.4 SMCR of *N*-heteroaryl bromides and *N*-heteroarylboronic acids[a]

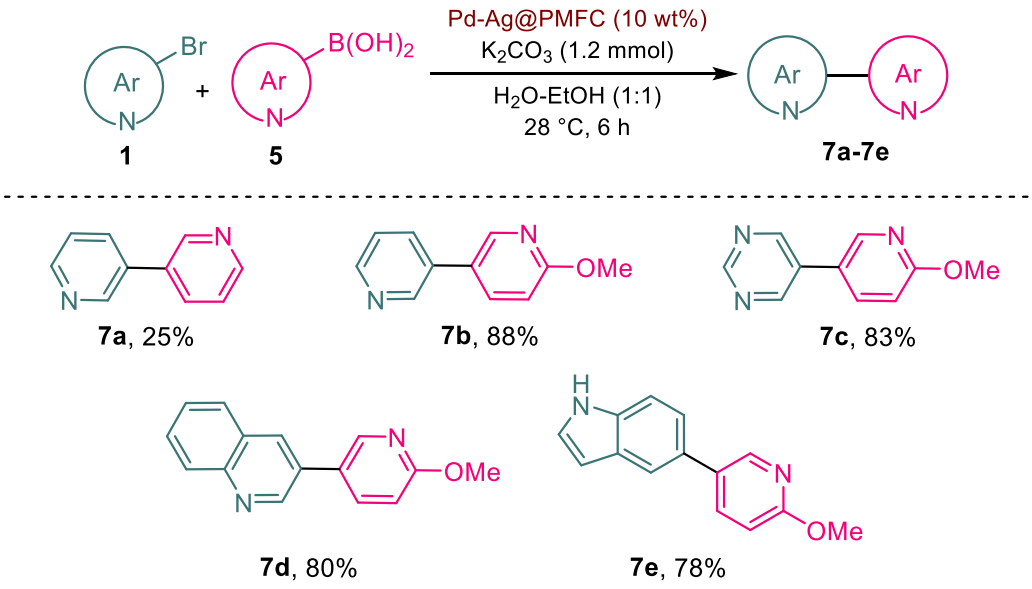

[a]Reaction conditions: **1** (0.5 mmol), **5** (0.6 mmol), Pd-Ag@PMFC (10 wt%, 0.001 mmol of Pd), K_2CO_3 (1.2 mmol), H_2O-EtOH 1:1 (4 mL), rt (28 °C), time (6 h); the yields reported are the isolated yields.

5.2.5 Hot-Filtration Test

The heterogeneity of the present catalyst and the real active species in the catalytic reaction was determined by performing a hot filtration test. Pd-Ag@PMFC (10 wt%) was pre-treated with K_2CO_3 (1.2 mmol) in H_2O-EtOH 1:1 (4 mL) in a round bottom flask at 28 °C. After 2 h, the solid catalyst phase was filtered off using Whatman filter paper (grade 41). The filtrate was collected in another round-bottom flask and employed for Suzuki-Miyaura coupling of **1a** (0.5 mmol) and **2a** (0.6 mmol) for 10 h. However, only a trace amount of product (**3a**) formation was detected even after an

extended reaction time. The ICP-OES analysis of the liquid phase reveals a residual amount (less than 0.01 ppm) of leached Pd and Ag species in the reaction medium. This inferior leaching suggests the heterogeneous nature of the active catalyst species.

5.2.6 Reusability test

For any heterogeneous system, defining its reusability is vital from the perspective of green and sustainable chemistry. Thus, the present catalyst was screened for recyclability employing two different series of reactions: **A**: 4-bromonitrobenzene (**4e**) and phenylboronic acid (**2a**); **B**: 3-bromopyridine (**1a**) and phenylboronic acid (**2a**) based on the optimized condition (Table **5.1**, entry **13**). Comparing both the cases containing aryl or heteroaryl substrates, the catalyst was found to be reusable for at least six successive reaction cycles demonstrated in Figure **5.9**.

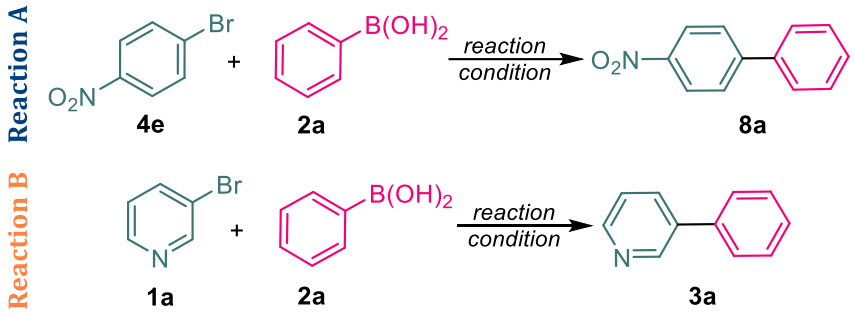

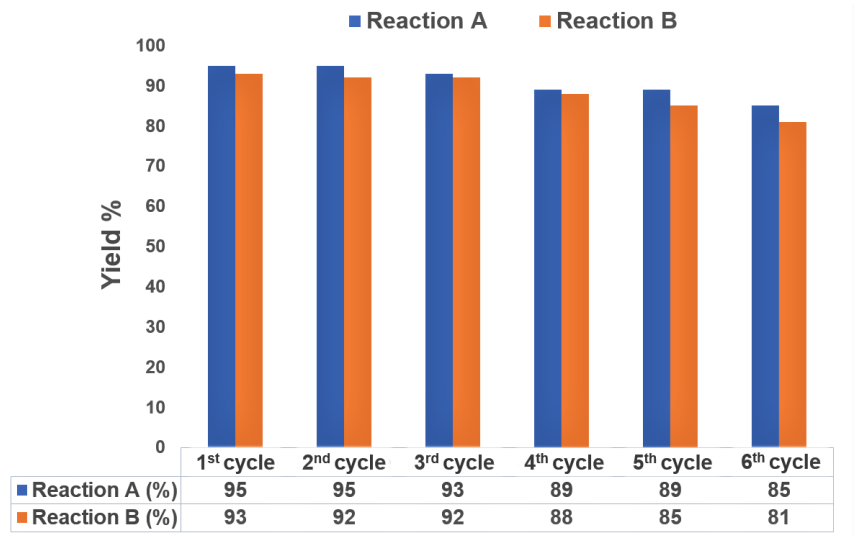

	1st cycle	2nd cycle	3rd cycle	4th cycle	5th cycle	6th cycle
Reaction A (%)	95	95	93	89	89	85
Reaction B (%)	93	92	92	88	85	81

[a]Reaction conditions: **1a/4e** (0.5 mmol), **2a** (0.6 mmol), Pd-Ag@PMFC (10 wt%, 0.001 mmol of Pd), K_2CO_3 (1.2 mmol), H_2O-EtOH 1:1 (4 mL), rt (28 °C); reaction time: **A**: 25 min; **B**: 6 h.

Figure 5.9 Reusability test for Pd-Ag@PMFC

As shown in Figure **5.9**, it is evident that the recovery after each catalytic cycles yield a very low efficiency drop. Although the presence of *N*-heteroatom is expected to cause catalyst deactivation by adsorbing on active sites, but in the present system, the catalyst could be successfully re-cycled without significant loss of catalytic activity. Thus, bi-metallization of Pd with Ag is likely to improve their resistance to poisoning [50].

5.2.7 Characterization of the Recovered Catalyst

The TEM image of the recovered Pd-Ag@PMFC catalyst is shown in Figure **5.10**. The images show that the spherical NCs are embedded on the cellulose surface (Figure **5.10a-b**). The average size of the NCs appears similar to the fresh catalyst (Figure **5.10c-d**). This indicates that the formed bi-metallic NCs retained their structural integrity after repeated recovery and reuse, remaining intact, demonstrating its stability. Moreover, HRTEM images also reveal the presence of crystal planes with lattice spacings of 0.137 nm and 0.117 nm corresponding to the (220) and (311) reflections of Pd and a plane at 0.201 nm for Ag, respectively (Figure **5.10e**). The SAED pattern shows well-resolved crystalline fringes corresponding to the (111), (200), (220), and (311) crystallographic planes of Pd-Ag NCs (Figure **5.10f**).

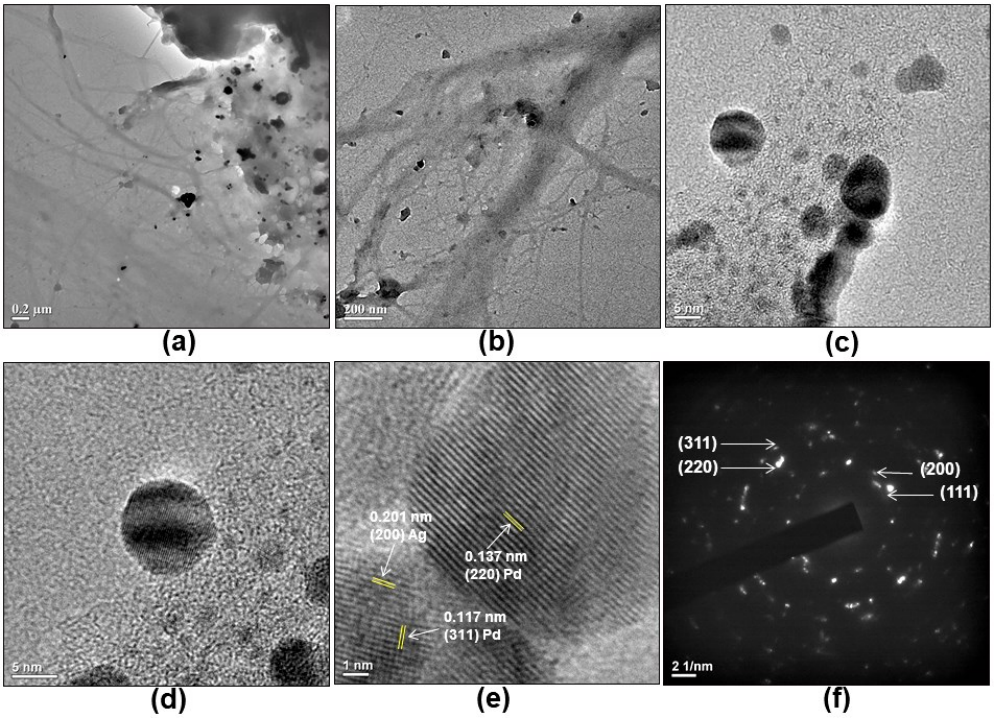

Figure 5.10 (a-d) TEM images, (e) HRTEM image, and (f) SAED pattern, of the recovered Pd-Ag@PMFC catalyst

The XPS analysis was also performed for the recovered Pd-Ag@PMFC catalyst (Figure **5.11**) and the high-resolution deconvoluted Pd 3d spectrum is shown in Figure **5.11a**. The binding energy peaks at 334.8 eV and 340.3 eV corresponds to the Pd(0), and peaks at 337.7 eV and 342.6 eV correspond to the Pd(II), respectively. The binding energy peak intensity for Pd(II) is increased after the fifth cycle, indicating that the catalyst is more oxidized after repeated catalytic runs. The peak position and intensity for high-resolution Ag 3d spectrum remain unchanged for recycled Pd-Ag@PMFC catalyst (Figure **5.11b**).

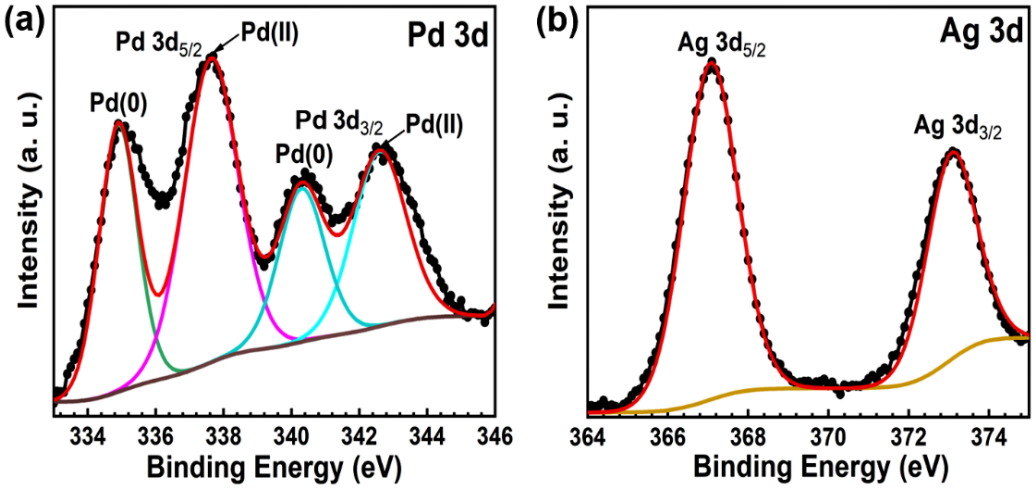

Figure 5.11 Deconvoluted high-resolution XPS spectra of (a) Pd 3d, (b) Ag 3d, of the recovered Pd-Ag@PMFC catalyst

5.2.8 Catalytic Role of Pd-Ag@PMFC in SMCR

The present system demonstrated considerable improvement in SMCR of *N*-heteroaryl compounds in terms of catalytic efficiency, milder reaction conditions, product yield, reusability and stability employing Pd-Ag@PMFC catalyst. Therefore, to determine the origin of this catalytic enhancement and to elucidate the specific role of each component of Pd-Ag@PMFC in SMCR, following experiments were performed. At first the catalytic activity of commercial supported-Pd catalyst (10% Pd/C) was assessed (Table **5.5**, entry **1**), where only 20% product formation could be detected at 28 °C. However, when the catalytic ability of mono-metallic Pd@PMFC was evaluated, it produced 71% of the cross-coupled product (Table **5.5**, entry **2**). This outcome laid attention on the significant role of cellulose bio-polymer support in the process. On the other hand, Ag@PMFC merely failed to initiate the reaction (Table **5.5**, entry **3**), revealing the necessity of Pd for the reaction to proceed. Further,

to identify the active Ag species, the system was examined with both Ag(I) ion (Table **5.5**, entry **4**), and Ag(0) NPs (Table **5.5**, entry **5**) in presence of Pd@PMFC. Enhancement in the product formation was observed with Ag NPs, whereas selectivity towards homocoupling side-product increased, reducing the yield of desired product in presence of Ag(I). Following, a reaction was performed *via in situ* reduced Pd(0) and Ag(0) species (Table **5.5**, entry **6**) where 78% product formation was detected. The results inevitably highlighted the assistance of Ag(0) in Pd catalyzed SMCR.

Table 5.5 Comparative study of different metal combinations[a]

Entry	Catalyst system	Yield (%)[b] of **3a**
1	10% Pd/C	20
2	Pd@PMFC	71
3	Ag@PMFC	nr
4	Pd@PMFC + $AgNO_3$[c]	60
5	Pd@PMFC + Ag NPs[c]	80
6	$Pd(OAc)_2$[c]+ $AgNO_3$[c] + extract[d]	78
7	Pd-Ag@PMFC	93
8[e]	Pd-Ag@PMFC	35

[a]Reaction conditions: **1a** (0.5 mmol), **2a** (0.6 mmol), catalyst (10 wt%), K_2CO_3 (1.2 mmol), H_2O-EtOH (4 mL), rt (28 °C), 6 h, air; [b]isolated yield; [c]catalyst 0.001 mmol; [d]extract 2 mL; [e]in dark; nr (no reaction).

Pd metal is unequivocally one of the most active metals for SMCR. However, the simultaneous presence of a plasmonic metal Ag can allow a facile electronic interaction *via* visible light mediated localized surface plasmon resonance (LSPR) [51,52], increasing the inherent reactivity of Pd. The Fermi energy level of Ag(0) is higher in position than Pd(0), with work function (Φ) values: Pd (5.12 eV) and Ag (4.26 eV) [51]. Due to the existence of this charge heterogeneity at the interface of two metals, the plasmonic electrons generated on Ag can be transferred to Pd under visible light. To verify the presence of LSPR effect in our catalytic system, a control reaction was performed in dark (Table **5.5**, entry **8**). Suppression of product formation clearly justifies the visible light-assisted electron-transfer mechanism.

5.2.9 Plausible Mechanism

Based on the experimental evidences, a plausible mechanism is proposed in agreement with literature. Figure **5.12** shows the UV-vis spectrum of the Pd-Ag@PMFC catalyst.

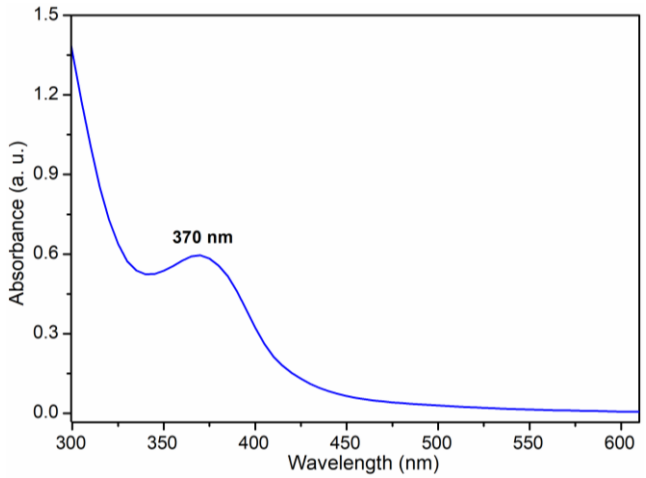

Figure 5.12 UV-vis spectrum of Pd-Ag@PMFC [0.01 g dispersed in H_2O-EtOH 1:1 (10 mL)]

The surface plasmon absorption of Ag NPs at around 370 nm implies the presence of photo-excited electrons of Ag on metal surface which are transferred to Pd. This activated electron-rich Pd centre is now more prone to oxidative addition of electrophile heteroaryl halide (**I**) in aqueous-organic phase [Pd(0)→Pd(II)] (Scheme **5.1**). This step is believed to be the rate-determining step leading to acceleration of the whole reaction pathway [53]. These energetic electrons are accumulated on the LUMO of electrophile through Pd centre, making the activation of heterocyclic halide counterpart easier compared to conventional Pd catalysis. The electrons return to the HOMO and finally back to the plasmonic Ag(0) after the activation of reactants [51]. In the transmetalation step, the nucleophile heteroarylboronic acid (**III**) initially in the basic-aqueous phase, enters the catalytic cycle by the assistance of hydrophilic PMFC support. The presence of numerous O−H functionalities in cellulose-polymer can assist in facile transfer of active boron-transmetalating species (**IV**) from basic aqueous to aqueous-organic phase, thereby accelerating the 'on-water' SMCR by acting as a phase-transfer agent [48]. In the reductive elimination step, the C−C coupled product (**VII**) is released from the Pd(II) species with the regeneration of Pd(0) to complete the catalytic cycle. Hence, the integration of Pd, Ag and hydrophilic

PMFC helped in amplifying the catalytic activity of Pd in 'on-water' SMCR by their multifunctional performance in various steps of catalytic pathway.

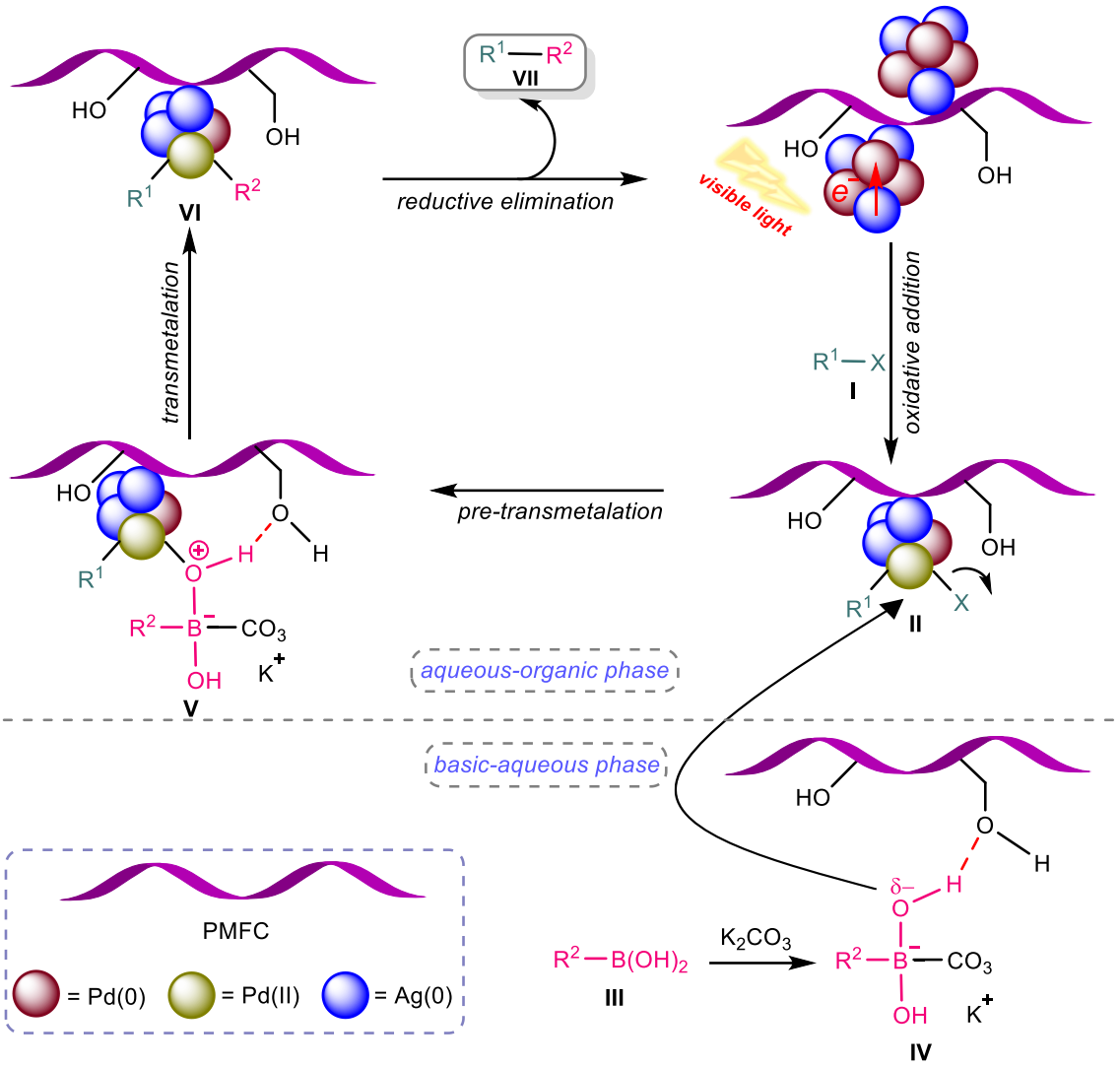

Scheme 5.1 Plausible mechanism for SMCR catalyzed by Pd-Ag@PMFC

5.2.10 Comparative Literature Analysis of Heterogeneous Catalysts Explored in SMCR of Heterocyclic Compounds

To determine the practical utility of the present methodology, a comparative literature analysis on the catalytic performance and recyclability of as-prepared Pd-Ag@PMFC in SMCR of heterocyclic moieties have been conducted. It can be noted that several methods available are based on homogeneous Pd catalysis [26-29,49]. The systems necessities the usage of expensive bulky ligands [29,49], and other additives to attain high efficacy, which are not advisable from sustainable chemistry point of view. A variety of other Pd-based heterogeneous catalysts have been devised for the

transformation (Table **5.6**).

Table 5.6 Comparison between Pd-Ag@PMFC catalyst and the previously reported methods in SMCR of heteroaromatic system

Entry [Ref.]	Catalyst	Conditions [Solvent/Base/ T (°C)/Time (h)]	Het(Ar)-substrates explored	Yield (%)	Reused cycles
1 [37]	PdNPs@NCmw	EtOH:H_2O/K_2CO_3/ 60/24	*N*-Het(Ar)-Br *N*-Het(Ar)-$B(OH)_2$	55-90	5[a]
2 [31]	10% Pd/C	50% *i*-PrOH/ Na_3PO_4/80/1-24	*N*-Het(Ar)-Br *S/O*-Het(Ar)-$B(OH)_2$	27-99	-
3 [25]	EcoPd	Glycerol/K_2CO_3/ 120/4	*N/S*-Het(Ar)-Br *N/S*-Het(Ar)-$B(OH)_2$	62-99	4[b]
4 [54]	Pd-M/C (M = Ag/Ni/Cu)	EtOH/ K_3PO_4/ 78/3	*S*-Het(Ar)-I	5-96	6[a]
5 [30]	[Pd–poly(AA)]	*i*-PrOH/K_2CO_3/ 90/5-14	*N/S*-Het(Ar)-Br *N/S*-Het(Ar)-$B(OH)_2$	63-83	3[a]
6 [32]	$Pd_{17}Se_{15}$	DMF:H_2O/K_2CO_3/ 110/13-30	*N*-Het(Ar)-Cl/Br	60-94	-
7 [33]	7% Pd/WA30	H_2O:dioxane/ NaOH/80/14	*N*-Het(Ar)-Cl/Br/I *O*-Het(Ar)-$B(OH)_2$	34-85	-
8	Pd-Ag@PMFC (Present work)	EtOH:H_2O/K_2CO_3/ 28/6	*N*-Het(Ar)-Br *N*-Het(Ar)-$B(OH)_2$	74-93	6[a][b]

[a]Reused only in arylated substrates; [b]Reused in heteroarylated substrates.

It can be noticed that most of the methods require higher reaction temperature (Table **5.6**, entries **1-7**) and longer reaction time (Table **5.6**, entries **1**, **2**, **6**) to achieve maximum catalytic activity in heterocyclic systems. Also, the utility of substates bearing heterocyclic core on the boron transmetalation partners are limited (Table **5.6**, entries **4**, **6**). Another bimetallic system using Pd-M/C (M = Ag/Ni/Cu) was found however showing only one heteroaryl substrate scope with 2-iodothiophene [54]. In terms of recyclability of the catalyst, most of the catalytic studies are limited to only conventional arylated substrates (Table **5.6**, entries **1**, **4**, **5**), may be due to the possibility of catalyst poisoning with heteroarylated substrates. Thus, compared to many reported methods, present Pd-Ag bimetallic synergy over the hydrophilic

biopolymer support offers additional properties for efficient exploration in nitrogen-rich heterocycles from the green and sustainable chemistry dimensions.

5.3 Summary

This chapter unfolds a sustainable and biocompatible approach for the extraction of micro-dimensional cellulose fibers from biomass waste using a simple ethanol-water filtration technique. The pomegranate peel derived cellulose micro-fibers presented as an admirable support matrix for bimetallic Pd-Ag nanoparticles. The synergistic visible-light harvesting and electronically interacting centres developed a novel plasmon-enhanced photocatalyst in promoting Suzuki-Miyaura coupling in exciting nitrogen heterocycles at room temperature under visible light.

The methodology highlighted an environment-friendly and hassle-free process of extraction of a potential green material-cellulose at lower cost with reduced energy and devoid of any toxic chemical consumption. Also creating new-dimensions towards heterogeneous photocatalysis as a promising "green" technology and a renewable energy source. Hence offering better scopes and perspectives for up-scaling productions of nanostructured materials for accessing desirable applications in a green and bio-economic consent.

5.4 Experimental Section

5.4.1 General Information

Reactions were carried out in Tarsons spinot digital magnetic stirrer and EYELA Process Station Personal Synthesizer PPS-CTRL1 under standard conditions. Analytical thin-layer chromatography (TLC) was carried out on Merck silica gel $60F_{254}$ plates using short wave (254 nm) UV light. Column chromatography purifications were performed over silica gel (100-200 mesh) and ethyl acetate/hexane as eluent. ^{1}H and ^{13}C NMR spectra were recorded on a JEOL JNM 400ECS NMR spectrometer (400 and 100 MHz respectively) using $CDCl_3$ as solvent and TMS as internal standard. The raw data of NMR were processed by MestReNova software. Chemical shifts (δ) are reported in ppm relative to the residual peak of the solvent ($CDCl_3$: ^{1}H NMR, δ = 7.25 ppm and sometimes δ = 1.56 ($CDCl_3$-water); and ^{13}C NMR, δ = 77.0 ppm) and TMS (0 ppm). Multiplicities are indicated as: s (singlet), d

(doublet), t (triplet), q (quartet), m (multiplet), dd (doublet of doublets) and br (broad). Coupling constants (*J* values) are given in hertz (Hz). All chemicals used were purchased commercially from either Sigma Aldrich, Merck or Alfa Aesar and used without further purification. Solvents used for extraction and chromatographic separations were distilled prior to use. The reactions were performed under general lighting conditions of the laboratory (average intensity value 2.92 W/m^2) recorded on a solar power meter (Model: KM-SPM-11).

5.4.2 Preparation of Catalysts

5.4.2.1 ***Preparation of PMFC:*** 20 g of waste peels of pomegranate fruit were collected and washed properly, finely chopped, ground and mixed with 100 mL distilled water. The water extract of fruit peel was filtered using Whatman filter paper (grade 41) and stored in refrigerator. Then, the peel residue on the filter paper was washed with 300 mL distilled water-ethanol 1:1 (v/v) mixture and allowed to dry in vacuum. The finely powdered white mass obtained was designated as PMFC.

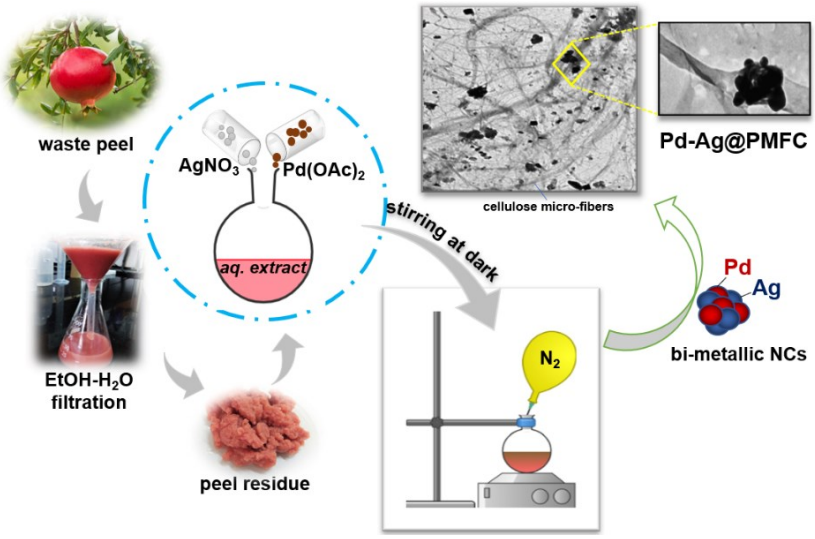

Figure 5.13 Schematic preparation method of Pd-Ag@PMFC from waste pomegranate peels

5.4.2.2 ***Preparation of Pd-Ag@PMFC:*** 4 g dried powder of PMFC was mixed with 20 mL of aqueous peel extract in a 50 mL round-bottom flask. To the mixture, 50 mM (0.112 g) $Pd(OAc)_2$ and 50 mM (0.085 g) $AgNO_3$ were added. The mixture was completely de-gassed and charged with N_2 gas. The reaction flask was covered with black paper and stirred at room temperature for 72 h. A gradual change in the color

of the solution from brown to black indicated the reduction of Pd^{2+} and Ag^{+} ions to Pd^{0} and Ag^{0} respectively. Thereafter, the mixture was centrifuged (600 rpm) and washed with water and ethanol and dried under vacuum to obtain the bi-metal loaded Pd-Ag@PMFC.

5.4.2.3 ***Preparation of Pd@PMFC and Ag@PMFC:*** As mentioned above for Pd-Ag@PMFC, same procedure was followed for Pd@PMFC and Ag@PMFC using 2 g PMFC with 10 mL aqueous extract and 50 mM $Pd(OAc)_2$ or $AgNO_3$ respectively.

5.4.3 Characterization of Catalysts

The powder XRD patterns were measured with the help of a Rigaku MultiFlex instrument using a nickel-filtered Cu Kα radiation source operating at a wavelength of 0.154 nm. The surface structure and morphology of the catalyst were observed by SEM (model: JEOL JSM 6390 LV) and TEM (model: JEOL JEM 2100 at 200 kV) analyses. The elemental composition of the nanostructure was determined by EDX analysis using the same SEM instrument. XPS measurements were carried out using a Thermo-Scientific ESCALAB Xi+ spectrometer with a monochromatic Al Kα X-ray source (1486.6 eV) and a spherical energy analyzer that operates in the CAE mode. The CAE for the survey spectrum is 200 eV and for high-resolution spectra is 50 eV. FT-IR spectra were recorded on a PerkinElmer Frontier MIR/FIR spectrometer, the wavenumbers (ν) of recorded IR signals are reported in cm^{-1}. The real content of Ag and Pd was determined by ICP-OES analysis on an ACROS ICP spectrometer. TGA was performed on a Shimadzu 60 thermal analyzer at a heating rate of 10 °C min^{-1} under continuous nitrogen flow. The BET surface area and porosity were measured, and the N_2 adsorption-desorption isotherms were recorded with a Quanta Chrome Novae-2200 surface area analyzer. UV-Vis spectrum was recorded on Shimadzu UV-2600i spectrophotometer.

5.4.4 General Procedure for SMCR of Heteroaryl Compounds

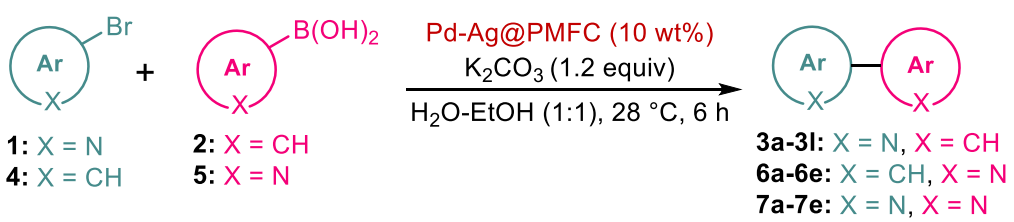

In a 50 mL round-bottom flask, a mixture of **1**/**4** (0.5 mmol), **2**/**5** (0.6 mmol), Pd-Ag@PMFC (10 wt%, 0.008 g) and K_2CO_3 (1.2 mmol) were stirred in H_2O-EtOH 1:1 (4 mL) at rt (28 °C). After completion of reaction (confirmed by TLC), the reaction mixture was diluted with distilled water and extracted with ethyl acetate, dried over anhydrous Na_2SO_4 and concentrated under reduced pressure. The crude product was purified by column chromatography to give the corresponding cross-coupling products (**3a-3l**, **6a-6e**, **7a-7e**).

For ***reusability experiments***, the heterogeneous catalyst particles were recovered from the reaction media by centrifugation (600 rpm) and subsequently washed with water and ethyl acetate. The resultant catalyst particles were dried under vacuum and subjected to subsequent reaction runs.

5.5 Characterization Data of the Products

3-Phenylpyridine

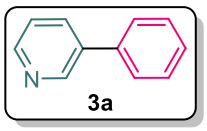

Obtained as colorless liquid, 73 mg, 93% yield; ^{1}H NMR (400 MHz, $CDCl_3$), δ (ppm): 8.85 (d, J = 2.6 Hz, 1H), 8.59 (dd, J = 4.9, 1.6 Hz, 1H), 7.89-7.86 (m, 1H), 7.59-7.57 (m, 2H), 7.50-7.46 (m, 2H), 7.42-7.35 (m, 2H); ^{13}C{^{1}H} NMR (100 MHz, $CDCl_3$), δ (ppm): 148.4, 148.2, 137.7, 136.6, 134.4, 129.0, 128.1, 127.1, 123.4.

3-(4-Methoxyphenyl)pyridine

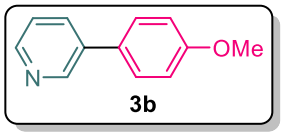

Obtained as white solid, 81 mg, 88% yield; ^{1}H NMR (400 MHz, $CDCl_3$), δ (ppm): 8.82 (d, J = 1.5 Hz, 1H), 8.54 (dd, J = 4.8, 1.7 Hz, 1H), 7.84-7.81 (m, 1H), 7.51 (d, J = 8.9 Hz, 2H), 7.33 (dd, J = 7.4, 4.4 Hz, 1H), 7.01 (d, J = 8.9 Hz, 2H), 3.85 (s, 3H); ^{13}C{^{1}H} NMR (100 MHz, $CDCl_3$), δ (ppm): 159.7, 147.8, 147.7, 136.2, 133.8, 130.1, 128.1, 123.5, 114.5, 55.3.

3-(4-(tert-Butyl)phenyl)pyridine

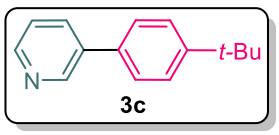

Obtained as colorless liquid, 94 mg, 89% yield; ^{1}H NMR (400 MHz, $CDCl_3$), δ (ppm): 8.85 (d, J = 2.2 Hz, 1H), 8.57 (dd, J = 4.9, 1.7 Hz, 1H), 7.92-7.89 (m, 1H), 7.54-7.49 (m, 4H), 7.38 (dd, J = 7.9, 4.9 Hz, 1H), 1.35 (s, 9H); ^{13}C{^{1}H} NMR (100 MHz, $CDCl_3$), δ (ppm): 151.4, 147.4, 147.3, 136.8, 134.7, 134.5, 126.7, 126.0, 123.7, 34.5, 31.0.

3-(4-Chlorophenyl)pyridine

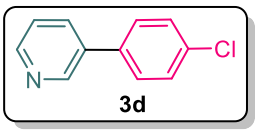

Obtained as colorless liquid, 77 mg, 81% yield; ^{1}H NMR (400 MHz, $CDCl_3$), δ (ppm): 8.83 (d, J = 2.6 Hz, 1H), 8.61 (dd, J = 4.8, 1.6 Hz, 1H), 7.89-7.86 (m, 1H), 7.52-7.39 (m, 5H); ^{13}C{^{1}H} NMR (100 MHz, $CDCl_3$), δ (ppm): 148.0, 147.4, 135.9, 135.8, 134.7, 134.5, 129.3, 128.3, 123.8.

5-Phenylpyrimidine

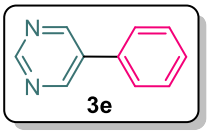

Obtained as colorless liquid, 73 mg, 93% yield; ^{1}H NMR (400 MHz, $CDCl_3$), δ (ppm): 9.21 (s, 1H), 8.96 (s, 2H), 7.60-7.47 (m, 5H); ^{13}C{^{1}H} NMR (100 MHz, $CDCl_3$), δ (ppm): 157.3, 154.8, 134.2, 134.1, 129.3, 128.9, 126.8.

5-(4-Methoxyphenyl)pyrimidine

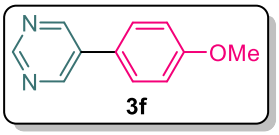

Obtained as white solid, 80 mg, 88% yield; ^{1}H NMR (400 MHz, $CDCl_3$), δ (ppm): 9.16 (s, 1H), 8.92 (s, 2H), 7.53 (d, J = 8.8 Hz, 2H), 7.05 (d, J = 8.8 Hz, 2H), 3.88 (s, 3H); ^{13}C{^{1}H} NMR (100 MHz, $CDCl_3$), δ (ppm): 160.4, 156.8, 154.3, 133.9, 128.1, 126.5, 114.7, 55.4.

5-(4-(tert-Butyl)phenyl)pyrimidine

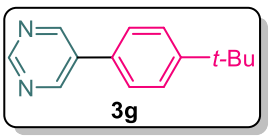

Obtained as colorless liquid, 90 mg, 85% yield; ^{1}H NMR (400 MHz, $CDCl_3$), δ (ppm): 9.19 (s, 1H), 8.95 (s, 2H), 7.57-7.52 (m, 4H), 1.37 (s, 9H); ^{13}C{^{1}H} NMR (100 MHz, $CDCl_3$), δ (ppm): 157.4, 154.7, 152.3, 134.1, 131.2, 126.7, 126.4, 34.7, 31.2.

5-(4-Chlorophenyl)pyrimidine

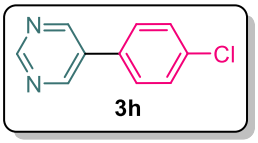

Obtained as colorless liquid, 76 mg, 80% yield; ^{1}H NMR (400 MHz, $CDCl_3$), δ (ppm): 9.22 (s, 1H), 8.93 (s, 2H), 7.54-7.49 (m, 4H); ^{13}C{^{1}H} NMR (100 MHz, $CDCl_3$), δ (ppm): 157.6, 154.6, 135.3, 133.1, 132.6, 129.6, 128.1.

5-(4-Fluorophenyl)pyrimidine

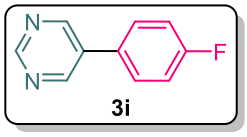

Obtained as colorless liquid, 70 mg, 81% yield; ^{1}H NMR (400 MHz, $CDCl_3$), δ (ppm): 9.20 (s, 1H), 8.92 (s, 1H), 7.57-7.53 (m, 2H), 7.25-7.19 (m, 2H); ^{13}C{^{1}H} NMR (100 MHz, $CDCl_3$), δ (ppm):

163.5 (d, *J* = 250.2 Hz), 157.4, 154.7, 133.5, 130.4, 128.8 (d, *J* = 5.8 Hz), 116.6 (d, *J* = 21.1 Hz).

3-Phenylquinoline

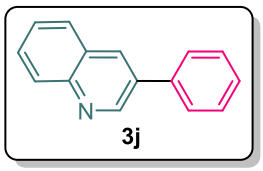

Obtained as colorless liquid, 85 mg, 83% yield; ^{1}H NMR (400 MHz, $CDCl_3$), δ (ppm): 9.20 (d, *J* = 2.2 Hz, 1H), 8.31 (d, *J* = 2.3 Hz, 1H), 8.16 (d, *J* = 8.5 Hz, 1H), 7.89 (d, *J* = 8.2 Hz, 1H), 7.75-7.71 (m, 3H), 7.60-7.52 (m, 3H), 7.47-7.42 (m, 1H); ^{13}C{^{1}H} NMR (100 MHz, $CDCl_3$), δ (ppm): 149.9, 147.3, 137.9, 133.8, 133.2, 129.4, 129.19, 129.15, 128.1, 128.01, 127.98, 127.4, 127.0.

5-(m-Tolyl)-1H-indole

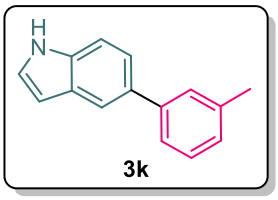

Obtained as colorless liquid, 88 mg, 86% yield; ^{1}H NMR (400 MHz, $CDCl_3$), δ (ppm): 8.05 (br s, 1H), 7.92 (m, 1H), 7.54-7.49 (m, 3H), 7.44-7.37 (m, 2H), 7.21-7.18 (m, 2H), 6.65-6.64 (m, 1H), 2.49 (s, 3H); ^{13}C{^{1}H} NMR (100 MHz, $CDCl_3$), δ (ppm): 142.5, 138.2, 135.2, 133.4, 128.5, 128.3, 127.0, 124.84, 124.75, 124.4, 121.8, 119.2, 111.1, 103.0, 21.5.

2-Methoxy-5-(4-methoxyphenyl)pyridine

Obtained as white solid, 90 mg, 85% yield; ^{1}H NMR (400 MHz, $CDCl_3$), δ (ppm): 8.34 (d, *J* = 3.0 Hz, 1H), 7.73 (dd, *J* = 8.6, 2.6 Hz, 1H), 7.45-7.43 (m, 2H), 6.99-6.95 (m, 2H), 6.79 (dd, *J* = 8.4, 0.8 Hz, 1H), 3.96 (s, 3H), 3.84 (s, 3H); ^{13}C{^{1}H} NMR (100 MHz, $CDCl_3$), δ (ppm): 163.1, 159.1, 144.4, 137.2, 130.3, 129.7, 127.7, 114.3, 110.7, 55.3, 53.5.

2-Methoxy-5-(4-nitrophenyl)pyridine

Obtained as yellow solid, 102 mg, 89% yield; ^{1}H NMR (400 MHz, $CDCl_3$), δ (ppm): 8.44 (dd, *J* = 2.6, 0.7 Hz, 1H), 8.36-8.27 (m, 2H), 7.83-7.77 (m, 1H), 7.72-7.65 (m, 2H), 6.86 (dd, *J* = 8.7, 0.7 Hz, 1H), 3.99 (s, 3H); ^{13}C{^{1}H} NMR (100 MHz, $CDCl_3$), δ (ppm): 164.6, 147.0, 145.6, 144.4, 137.3, 128.3, 127.1, 124.3, 111.4, 53.8.

1-(4-(6-Methoxypyridin-3-yl)phenyl)ethan-1-one

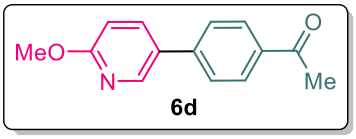

6d

Obtained as colorless liquid, 92 mg, 81% yield; ^{1}H NMR (400 MHz, $CDCl_3$), δ (ppm): 8.44 (d, J = 2.6 Hz, 1H), 8.04 (d, J = 8.1 Hz, 2H), 7.83 (dd, J = 8.6, 2.5 Hz, 1H), 7.63 (d, J = 8.1 Hz, 2H), 6.85 (d, J = 8.6 Hz, 1H), 4.00 (s, 3H), 2.64 (s, 3H); ^{13}C{^{1}H} NMR (100 MHz, $CDCl_3$), δ (ppm): 197.5, 164.2, 145.3, 142.5, 137.3, 135.8, 129.1, 126.5, 111.0, 99.8, 53.7, 26.6.

5-(o-Tolyl)-1H-indole

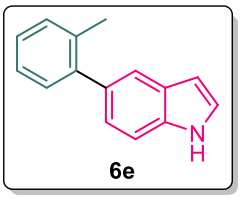

6e

Obtained as colorless liquid, 83 mg, 81% yield; ^{1}H NMR (400 MHz, $CDCl_3$), δ (ppm): 8.07 (br s, 1H), 7.59 (m, 1H), 7.39 (d, J = 8.4 Hz, 1H), 7.33-7.24 (m, 4H), 7.21-7.16 (m, 2H), 6.59-6.57 (m, 1H), 2.32 (s, 3H); ^{13}C{^{1}H} NMR (100 MHz, $CDCl_3$), δ (ppm): 143.0, 135.7, 134.7, 133.8, 130.3, 130.2, 127.7, 126.7, 125.6, 124.7, 123.8, 121.0, 110.4, 102.7, 20.7.

6-Methoxy-3,3'-bipyridine

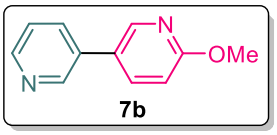

7b

Obtained as colorless liquid, 81 mg, 88% yield; ^{1}H NMR (400 MHz, $CDCl_3$), δ (ppm): 8.80 (d, J = 2.4 Hz, 1H), 8.60 (dd, J = 4.8, 1.6 Hz, 1H), 8.39 (d, J = 2.6 Hz, 1H), 7.84-7.78 (m, 2H), 7.38 (dd, J = 7.9, 4.8 Hz, 1H), 6.87 (d, J = 8.6 Hz, 1H), 3.99 (s, 3H); ^{13}C{^{1}H} NMR (100 MHz, $CDCl_3$), δ (ppm): 164.1, 148.5, 147.7, 145.1, 137.3, 133.9, 133.5, 126.7, 123.7, 111.2, 53.7.

5-(6-Methoxypyridin-3-yl)pyrimidine

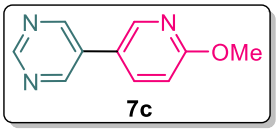

7c

Obtained as colorless liquid, 77 mg, 83% yield; ^{1}H NMR (400 MHz, $CDCl_3$), δ (ppm): 9.21 (s, 1H), 8.92 (s, 2H), 8.40 (d, J = 2.6 Hz, 1H), 7.79 (dd, J = 8.6, 2.6 Hz, 1H), 6.90 (d, J = 8.6 Hz, 1H), 4.00 (s, 3H); ^{13}C{^{1}H} NMR (100 MHz, $CDCl_3$), δ (ppm): 164.7, 157.4, 154.4, 145.1, 137.0, 131.5, 123.2, 111.6, 53.8.

3-(6-Methoxypyridin-3-yl)quinoline

Obtained as colorless liquid, 94 mg, 80% yield; ^{1}H NMR (400 MHz, $CDCl_3$), δ (ppm): 9.12 (d, J = 2.1 Hz, 1H), 8.51 (d, J = 2.2 Hz, 1H), 8.22 (d, J = 2.1 Hz, 1H), 8.14 (d, J = 8.4

Hz, 1H), 7.89 (dd, *J* = 8.6, 2.6 Hz, 1H), 7.86 (d, *J* = 8.1 Hz, 1H), 7.74-7.70 (m, 1H), 7.59-7.55 (m, 1H), 6.89 (d, *J* = 8.6 Hz, 1H), 4.01 (s, 3H); $^{13}C\{^{1}H\}$ NMR (100 MHz, $CDCl_3$), *δ* (ppm): 164.0, 149.1, 147.2, 145.3, 137.4, 132.6, 130.6, 129.4, 129.1, 127.7, 127.0, 126.7, 111.3, 99.9, 53.6.

5-(6-Methoxypyridin-3-yl)-1H-indole

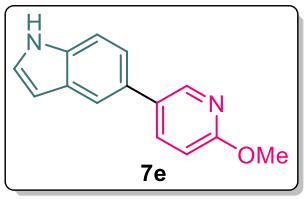

Obtained as colorless liquid, 86 mg, 78% yield; ^{1}H NMR (400 MHz, $CDCl_3$), *δ* (ppm): 8.44-8.41 (m, 2H), 7.84 (dd, *J* = 8.6, 2.6 Hz, 1H), 7.77 (s, 1H), 7.44 (d, *J* = 8.5 Hz, 1H), 7.35 (dd, *J* = 8.4, 1.8 Hz, 1H), 7.23 (dd, *J* = 3.3, 2.5 Hz, 1H), 6.82 (d, *J* = 8.5 Hz, 1H), 6.61-6.59 (m, 1H), 3.99 (s, 3H); $^{13}C\{^{1}H\}$ NMR (100 MHz, $CDCl_3$), *δ* (ppm): 163.0, 144.8, 138.0, 135.3, 131.5, 129.8, 128.4, 125.0, 121.3, 118.8, 111.5, 110.6, 102.9, 53.5.

5.6 Representative ^{1}H and $^{13}C\{^{1}H\}$ NMR spectra

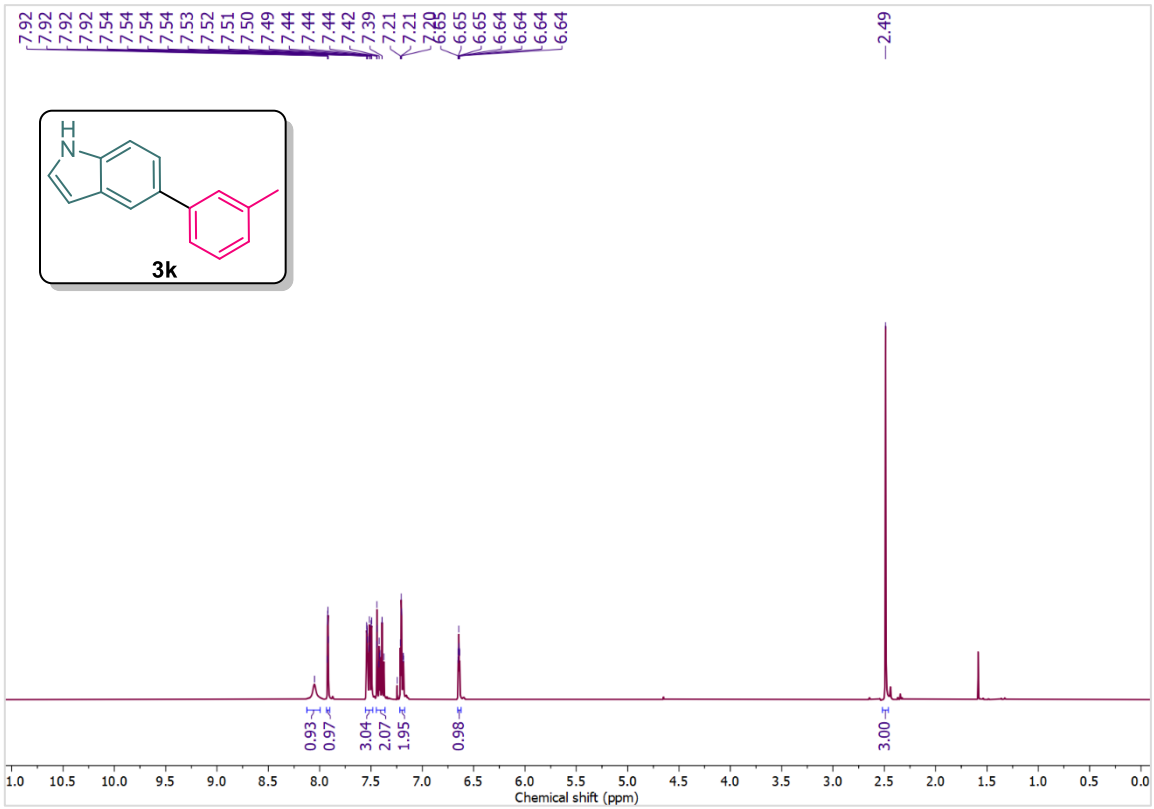

Figure 5.14 ^{1}H NMR (400 MHz) spectrum of **3k** in $CDCl_3$

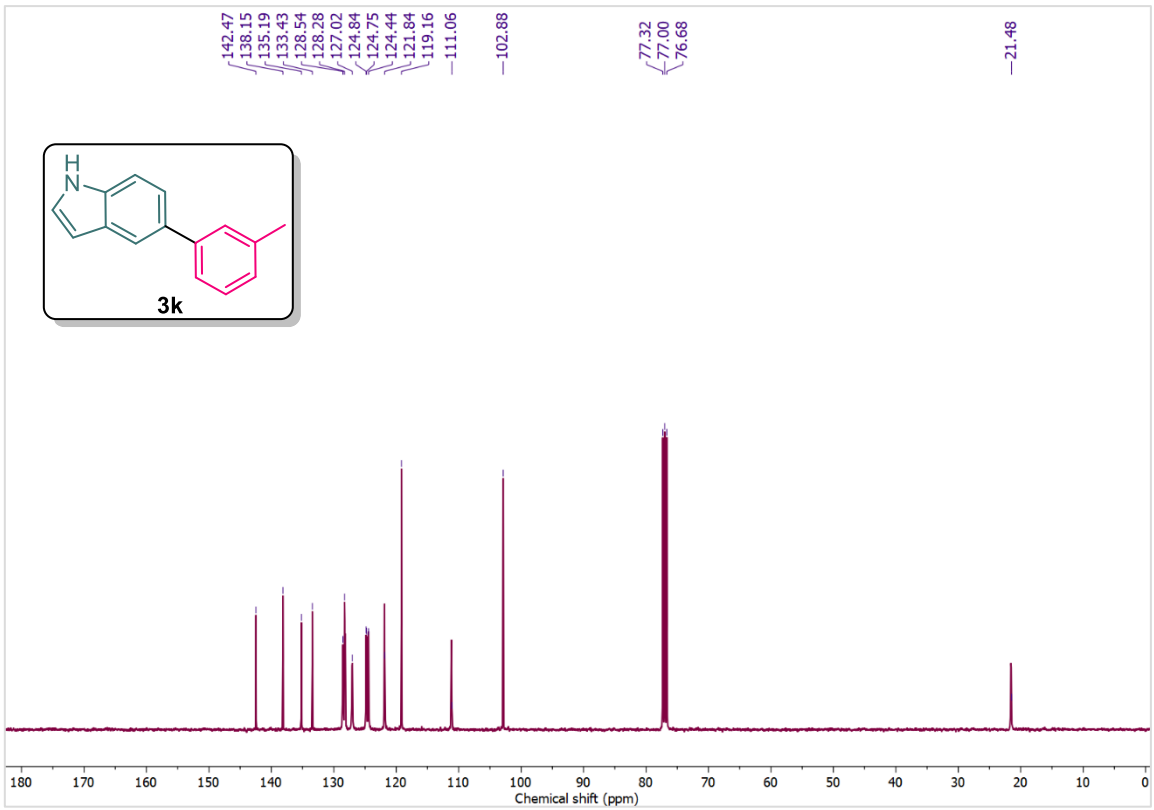

Figure 5.15 $^{13}C\{^{1}H\}$ NMR (100 MHz) spectrum of **3k** in $CDCl_3$

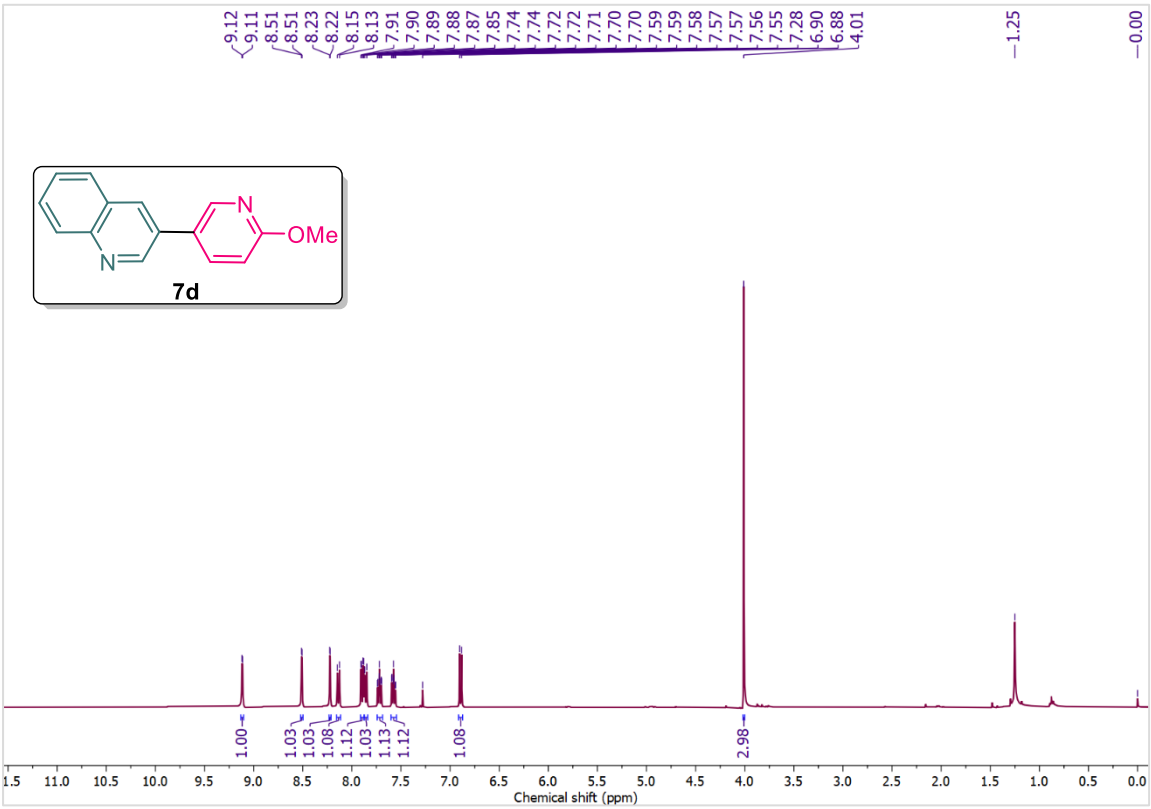

Figure 5.16 ^{1}H NMR (400 MHz) spectrum of **3k** in $CDCl_3$

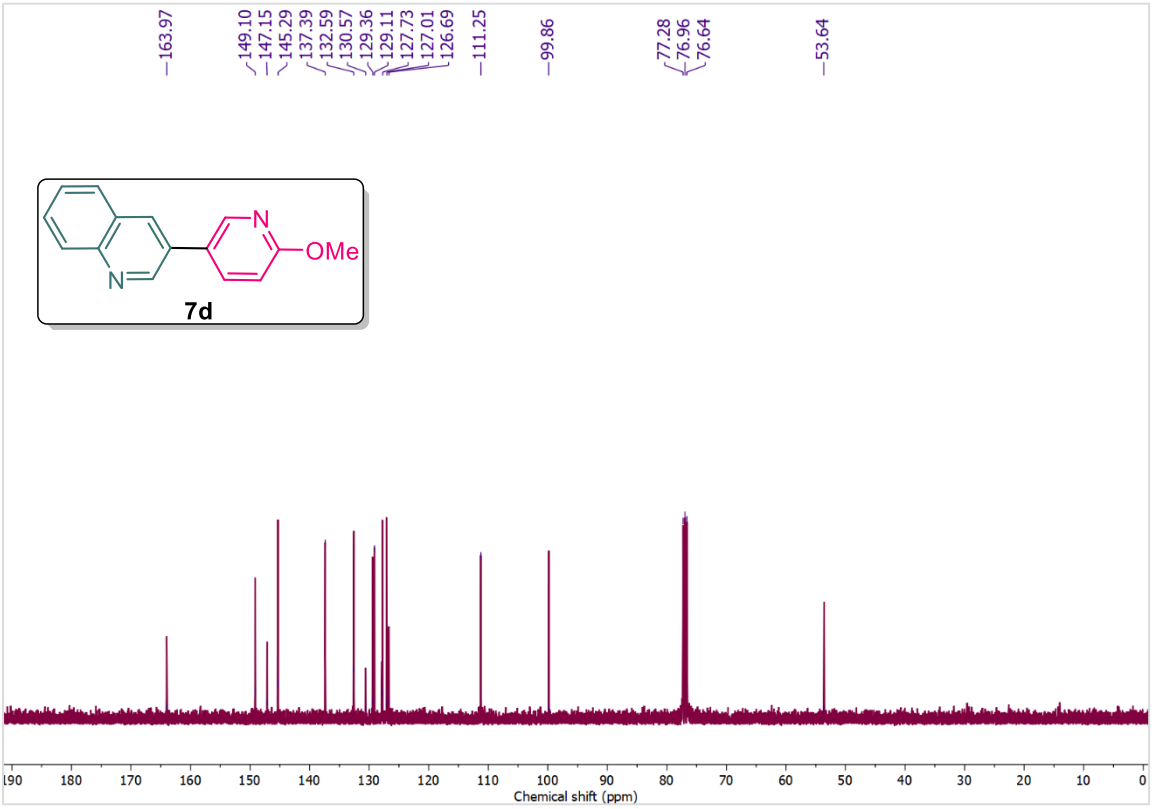

Figure 5.17 $^{13}C\{^{1}H\}$ NMR (100 MHz) spectrum of **3k** in $CDCl_3$

5.7 Bibliography

[1] Kadu, B. S. Suzuki-Miyaura cross coupling reaction: recent advancements in catalysis and organic synthesis. *Catalysis Science & Technology*, 11(4):1186-1221, 2021.

[2] Ayogu, J. I. and Onoabedje, E. A. Recent advances in transition metal-catalyzed cross-coupling of (hetero)aryl halides and analogues under ligand-free conditions. *Catalysis Science & Technology*, 9(19):5233-5255, 2019.

[3] Parandhaman, T., Dey, M. D., and Das, S. K. Biofabrication of supported metal nanoparticles: exploring the bioinspiration strategy to mitigate the environmental challenges. *Green Chemistry*, 21(20):5469-5500, 2019.

[4] Peter, Z. Order in cellulosics: historical review of crystal structure research on cellulose. *Carbohydrate Polymers*, 254:117417, 2021.

[5] Pandey, A. Pharmaceutical and biomedical applications of cellulose nanofibers: a review. *Environmental Chemistry Letters*, 19(3):2043-2055, 2021.

[6] Ventura-Cruz, S. and Tecante, A. Nanocellulose and microcrystalline cellulose from agricultural waste: review on isolation and application as reinforcement in polymeric matrices. *Food Hydrocolloids*, 118:106771, 2021.

[7] Kandathil, V., Kempasiddaiah, M., Sasidhar, B. S., and Patil, S. A. From agriculture residue to catalyst support; a green and sustainable cellulose-based dip catalyst for C–C coupling and direct arylation. *Carbohydrate Polymers*, 223:115060, 2019.

[8] Pei, X., Li, Y., Lu, L., Jiao, H., Gong, W., and Zhang, L. Highly dispersed Pd clusters anchored on nanoporous cellulose microspheres as a highly efficient catalyst for the Suzuki coupling reaction. *ACS Applied Materials & Interfaces*, 13(37):44418-44426, 2021.

[9] Wu, X., Lu, C., Zhou, Z., Yuan, G., Xiong, R., and Zhang, X. Green synthesis and formation mechanism of cellulose nanocrystal-supported gold nanoparticles with enhanced catalytic performance. *Environmental Science: Nano*, 1(1):71-79, 2014.

[10] Tavker, N., Gaur, U. K., and Sharma, M. Agro-waste extracted cellulose supported silver phosphate nanostructures as a green photocatalyst for

improved photodegradation of RhB dye and industrial fertilizer effluents. *Nanoscale Advances*, 2(7):2870-2884, 2020.

[11] Karami, S., Zeynizadeh, B., and Shokri, Z. Cellulose supported bimetallic Fe-Cu nanoparticles: a magnetically recoverable nanocatalyst for quick reduction of nitroarenes to amines in water. *Cellulose*, 25:3295-3305, 2018.

[12] Mamatha, G., Sowmya, P., Madhuri, D., Mohan Babu, N., Suresh Kumar, D., Vijaya Charan, G., Varaprasad, K., and Madhukar, K. Antimicrobial cellulose nanocomposite films with *in situ* generations of bimetallic (Ag and Cu) nanoparticles using Vitex negundo leaves extract. *Journal of Inorganic and Organometallic Polymers and Materials*, 31:802-815, 2021.

[13] Haslinger, S., Ye, Y., Rissanen, M., Hummel, M., and Sixta, H. Cellulose fibers for high-performance textiles functionalized with incorporated gold and silver nanoparticles. *ACS Sustainable Chemistry & Engineering*, 8(1):649-658, 2019.

[14] Picot-Allain, M. C. N. and Emmambux, M. N. Isolation, characterization, and application of nanocellulose from agro-industrial by-products: a review. *Food Reviews International*, 39(2):941-969, 2023.

[15] Sundarraj, A. A. and Ranganathan, T. V. A review on cellulose and its utilization from agro-industrial waste. *Drug Invention Today*, 10(1):89-94, 2018.

[16] Trache, D., Tarchoun, A. F., Derradji, M., Hamidon, T. S., Masruchin, N., Brosse, N., and Hussin, M. H. Nanocellulose: from fundamentals to advanced applications. *Frontiers in Chemistry*, 8:392, 2020.

[17] Onyianta, A. J., O'Rourke, D., Sun, D., Popescu, C. M., and Dorris, M. High aspect ratio cellulose nanofibrils from macroalgae *Laminaria hyperborea* cellulose extract *via* a zero-waste low energy process. *Cellulose*, 27:7997-8010, 2020.

[18] Usmani, Z., Sharma, M., Gupta, P., Karpichev, Y., Gathergood, N., Bhat, R., and Gupta, V. K. Ionic liquid-based pretreatment of lignocellulosic biomass for enhanced bioconversion. *Bioresource Technology*, 304:123003, 2020.

[19] Wang, H., Li, J., Zeng, X., Tang, X., Sun, Y., Lei, T., and Lin, L. Extraction of cellulose nanocrystals using a recyclable deep eutectic solvent. *Cellulose*, 27:1301-1314, 2020.

[20] Rizwan, M., Gilani, S. R., Durrani, A. I., and Naseem, S. Low temperature green extraction of *Acer platanoides* cellulose using nitrogen protected microwave

assisted extraction (NPMAE) technique. *Carbohydrate Polymers*, 272:118465, 2021.

[21] Pang, Z., Wang, P., and Dong, C. Ultrasonic pretreatment of cellulose in ionic liquid for efficient preparation of cellulose nanocrystals. *Cellulose*, 25:7053-7064, 2018.

[22] Sharma, G., Kumar, D., Kumar, A., Ala'a, H., Pathania, D., Naushad, M., and Mola, G. T. Revolution from monometallic to trimetallic nanoparticle composites, various synthesis methods and their applications: a review. *Materials Science and Engineering: C*, 71:1216-1230, 2017.

[23] Ayogu, J. I. and Onoabedje, E. A. Prospects and applications of palladium nanoparticles in the cross-coupling of (hetero)aryl halides and related analogues. *ChemistryOpen*, 10(4):430-450, 2021.

[24] Düfert, M. A., Billingsley, K. L., and Buchwald, S. L. Suzuki-Miyaura cross-coupling of unprotected, nitrogen-rich heterocycles: substrate scope and mechanistic investigation. *Journal of the American Chemical Society*, 135(34):12877-12885, 2013.

[25] Clavé, G., Pelissier, F., Campidelli, S., and Grison, C. Ecocatalyzed Suzuki cross coupling of heteroaryl compounds. *Green Chemistry*, 19(17):4093-4103, 2017.

[26] Kumar, M. R., Park, K., and Lee, S. Synthesis of amido-*N*-imidazolium salts and their applications as ligands in Suzuki-Miyaura reactions: coupling of hetero-aromatic halides and the synthesis of milrinone and irbesartan. *Advanced Synthesis & Catalysis*, 352(18):3255-3266, 2010.

[27] Guo, P., Zhang, H., Zhou, J., Gallou, F., Parmentier, M., and Wang, H. Micelle-enabled Suzuki-Miyaura cross-coupling of heteroaryl boronate esters. *The Journal of Organic Chemistry*, 83(14):7523-7527, 2018.

[28] Kassel, V. M., Hanneman, C. M., Delaney, C. P., and Denmark, S. E. Heteroaryl-heteroaryl, Suzuki-Miyaura, anhydrous cross-coupling reactions enabled by trimethyl borate. *Journal of the American Chemical Society*, 143(34):13845-13853, 2021.

[29] Ouyang, J. S., Li, Y. F., Huang, F. D., Lu, D. D., and Liu, F. S. The highly efficient Suzuki-Miyaura cross-coupling of (hetero)aryl chlorides and

(hetero)arylboronic acids catalyzed by "bulky-yet-flexible" palladium–PEPPSI complexes in air. *ChemCatChem*, 10(2):371-375, 2018.

[30] Islam, R. U., Witcomb, M. J., Scurrell, M. S., Van Der Lingen, E., Van Otterlo, W., and Mallick, K. Conjugated polymer stabilized palladium nanoparticles as a versatile catalyst for Suzuki cross-coupling reactions for both aryl and heteroaryl bromide systems. *Catalysis Science & Technology*, 1(2):308-315, 2011.

[31] Kitamura, Y., Sako, S., Udzu, T., Tsutsui, A., Maegawa, T., Monguchi, Y., and Sajiki, H. Ligand-free Pd/C-catalyzed Suzuki-Miyaura coupling reaction for the synthesis of heterobiaryl derivatives. *Chemical Communications*, 47:5069-5071, 2007.

[32] Rao, G. K., Kumar, A., Ahmed, J., and Singh, A. K. Palladacycle containing nitrogen and selenium: highly active pre-catalyst for the Suzuki-Miyaura coupling reaction and unprecedented conversion into nano-sized $Pd_{17}Se_{15}$. *Chemical Communications*, 46(32):5954-5956, 2010.

[33] Yamada, T., Jiang, J., Ito, N., Park, K., Masuda, H., Furugen, C., Ishida, M., Ōtori, S., and Sajiki, H. Development of facile and simple processes for the heterogeneous Pd-catalyzed ligand-free continuous-flow Suzuki-Miyaura coupling. *Catalysts*, 10(10):1209, 2020.

[34] Mudarra, Á. L., de Salinas, S. M., and Pérez-Temprano, M. H. Beyond the traditional roles of Ag in catalysis: the transmetalating ability of organosilver(I) species in Pd-catalysed reactions. *Organic & Biomolecular Chemistry*, 17(7):1655-1667, 2019.

[35] Hirakawa, K., Kaneko, T., and Toshima, N. Kinetics of spontaneous bimetallization between silver and noble metal nanoparticles. *Chemistry–An Asian Journal*, 13(15):1892-1896, 2018.

[36] Zhang, J., Huang, B., Shao, Q., and Huang, X. Highly active, selective, and stable direct H_2O_2 generation by monodispersive Pd-Ag nanoalloy. *ACS Applied Materials & Interfaces*, 10(25):21291-21296, 2018.

[37] Dewan, A., Sarmah, M., Bharali, P., Thakur, A. J., Boruah, P. K., Das, M. R., and Bora, U. Pd nanoparticles-loaded honeycomb-structured bio-nanocellulose as a heterogeneous catalyst for heteroaryl cross-coupling reaction. *ACS Sustainable Chemistry & Engineering*, 9(2):954-966, 2021.

[38] Sukri, S. N. A. M., Shameli, K., Wong, M. M. T., Teow, S. Y., Chew, J., and Ismail, N. A. Cytotoxicity and antibacterial activities of plant-mediated synthesized zinc oxide (ZnO) nanoparticles using *Punica granatum* (pomegranate) fruit peels extract. *Journal of Molecular Structure*, 1189:57-65, 2019.

[39] Musino, D., Rivard, C., Landrot, G., Novales, B., Rabilloud, T., and Capron, I. Hydroxyl groups on cellulose nanocrystal surfaces form nucleation points for silver nanoparticles of varying shapes and sizes. *Journal of Colloid and Interface Science*, 584:360-371, 2021.

[40] Goldmann, W. M., Ahola, J., Mikola, M., and Tanskanen, J. Solubility and fractionation of Indulin AT kraft lignin in ethanol-water media. *Separation and Purification Technology*, 209:826-832, 2019.

[41] Shankar, S. S., Ahmad, A., and Sastry, M. Geranium leaf assisted biosynthesis of silver nanoparticles. *Biotechnology Progress*, 19(6):1627-1631, 2003.

[42] Philip, D. Biosynthesis of Au, Ag and Au-Ag nanoparticles using edible mushroom extract. *Spectrochimica Acta Part A: Molecular and Biomolecular Spectroscopy*, 73(2):374-381, 2009.

[43] Adekoya, J. A., Dare, E. O., Mesubi, M. A., Nejo, A. A., Swart, H. C., and Revaprasadu, N. Synthesis of polyol-based Ag/Pd nanocomposites for applications in catalysis. *Results in Physics*, 4:12-19, 2014.

[44] Thirumavalavan, M., Lai, Y. L., and Lee, J. F. Fourier transform infrared spectroscopic analysis of fruit peels before and after the adsorption of heavy metal ions from aqueous solution. *Journal of Chemical & Engineering Data*, 56(5):2249-2255, 2011.

[45] Anfar, Z., Ait Ahsaine, H., Zbair, M., Amedlous, A., Ait El Fakir, A., Jada, A., and El Alem, N. Recent trends on numerical investigations of response surface methodology for pollutants adsorption onto activated carbon materials: a review. *Critical Reviews in Environmental Science and Technology*, 50(10): 1043-1084, 2020.

[46] Wang, X., Chen, J., Zeng, J., Wang, Q., Li, Z., Qin, R., Wu, C., Xie, Z., and Zheng, L. The synergy between atomically dispersed Pd and cerium oxide for enhanced catalytic properties. *Nanoscale*, 9(20):6643-6648, 2017.

[47] Zhao, Z., Wang, Y., Xu, J., and Wang, Y. Mesoporous Ag/TiO_2 nanocomposites with greatly enhanced photocatalytic performance towards degradation of methyl orange under visible light. *RSC Advances*, 5(73):59297-59305, 2015.

[48] Wang, M., Xue, H., Ju, F., and Yang, H. Acceleration of batch-type heterogeneous ligand-free Suzuki-Miyaura reactions with polymer composite supported Pd catalyst. *Scientific Reports*, 7(1):7006, 2017.

[49] Noël, T. and Musacchio, A. J. Suzuki-Miyaura cross-coupling of heteroaryl halides and arylboronic acids in continuous flow. *Organic Letters*, 13(19):5180-5183, 2011.

[50] Chen, M., Zhang, Z., Li, L., Liu, Y., Wang, W., and Gao, J. Fast synthesis of Ag-Pd@ reduced graphene oxide bimetallic nanoparticles and their applications as carbon–carbon coupling catalysts. *RSC Advances*, 4(58):30914-30922, 2014.

[51] Verma, P., Kuwahara, Y., Mori, K., and Yamashita, H. Pd/Ag and Pd/Au bimetallic nanocatalysts on mesoporous silica for plasmon-mediated enhanced catalytic activity under visible light irradiation. *Journal of Materials Chemistry A*, 4(26):10142-10150, 2016.

[52] Verma, P., Kuwahara, Y., Mori, K., and Yamashita, H. Synthesis and characterization of a Pd/Ag bimetallic nanocatalyst on SBA-15 mesoporous silica as a plasmonic catalyst. *Journal of Materials Chemistry A*, 3(37):18889-18897, 2015.

[53] Nemygina, N. A., Nikoshvili, L. Z., Tiamina, I. Y., Bykov, A. V., Smirnov, I. S., LaGrange, T., Kaszkur, Z., Matveeva, V. G., Sulman, E. M., and Kiwi-Minsker, L. Au Core-Pd shell bimetallic nanoparticles immobilized within hyper-cross-linked polystyrene for mechanistic study of Suzuki cross-coupling: homogeneous or heterogeneous catalysis. *Organic Process Research & Development*, 22(12):1606-1613, 2018.

[54] Kim, S. J., Oh, S. D., Lee, S., and Choi, S. H. Radiolytic synthesis of Pd-M (M = Ag, Ni, and Cu)/C catalyst and their use in Suzuki-type and Heck-type reaction. *Journal of Industrial and Engineering Chemistry*, 14(4);449-456, 2008.